Length-scales for efficient CFL conditions in high-order methods with distorted meshes: Application to local-timestepping for p-multigrid

Saumitra Joshi[a,*], Jiaqing Kou[b], Aurelio Hurtado de Mendoza[c], Kunal Puri[c], Charles Hirsch[c], Gonzalo Rubio[a,d], Esteban Ferrer[a,d]

[a]*ETSIAE, School of Aeronautics, Universidad Politécnica de Madrid, Plaza Cardenal Cisneros 3, Madrid E-28040, Spain.*
[b]*AIA, RWTH Aachen University, Wüllnerstraße 5a, 52062 Aachen, Germany*
[c]*Cadence Design Systems Limited, Chaussée de la Hulpe 189, Brussels B-1170, Belgium.*
[d]*Center for Computational Simulation, Universidad Politécnica de Madrid, Campus de Montegancedo, Boadilla del Monte, Madrid E-28660, Spain.*

ARTICLE INFO

ABSTRACT

We propose a strategy to estimate the maximum stable time-steps for explicit time-stepping methods for hyperbolic systems in a high-order flux reconstruction framework. The strategy is derived through a von-Neumann analysis (VNA) framework for the advection-diffusion equation on skewed two- and three-dimensional meshes. It directly incorporates the spatial polynomial- and mesh-discretization in estimating the convective and diffusive length-scales. The strategy is extended to the density-based Navier-Stokes system of equations, taking into account the omnidirectionality of the speed of sound.

We compare the performance of this strategy with three other popular choices of length-scales across a wide range of polynomial-orders, meshes of drastically varying cell-quality, and flow-physics. The proposed strategy shows robust behavior across all test-scenarios with limited variation of the maximum stable CFL-number (0.1 to 1) for polynomial-orders 1 through 10, unlike other strategies where the CFL-number varies sharply. Finally, we show the advantage of the proposed methodology for local-timestepping for p-multigrid through a RANS-modeled steady-state turbulent flow case, on a mesh with large disparity of mesh elements and aspect ratios.

Contents

1. Introduction

The growing prevalance of <u>C</u>omputational <u>F</u>luid <u>D</u>ynamics (CFD) across engineering disciplines continues to drive research towards more efficient and robust numerical methods [1]. Most methods employed in industry involve spatial discretization of the governing equations, followed by temporal discretization realized through time-integrators. Implicit time-integrators are known for their unconditional stability [2] but can be expensive and memory-intensive, particularly for high-order methods [3]. On the other hand, the computational efficiency of explicit time-integrators is restricted by stability-induced limits on their maximum step-size $\Delta t_{\max}$. In practice, $\Delta t_{\max}$ is estimated by a heuristic condition of the form [4, 5, 6, 7, 8]:

$$\Delta t = \mathfrak{C}\frac{\mathfrak{h}}{\|\boldsymbol{\psi}\|}. \tag{1}$$

where $\mathfrak{h}$ is an approximated characteristic length-scale, $\|\boldsymbol{\psi}\|$ is the physical rate of information propagation of the problem, and $\mathfrak{C}$ is a constant whose value is tuned (usually by trial-and-error on a case-to-case basis) to obtain

48 $\Delta t \approx \Delta t_{\max}$. Since $\|\boldsymbol{\psi}\|$ is known from the state of the problem, it is $\mathfrak{h}$ that causes the constant $\mathfrak{C}$ to differ from one

49 problem to another. In other words, if $\mathfrak{h}$ is computed correctly, then (1) will yield $\Delta t_{\max}$ for a fixed value of $\mathfrak{C}$ which

50 will be independent of the case.

51   The constant $\mathfrak{C}$ is typically referred to as the "CFL-number", even though it is used in the context of both con-

52 vective [6, 7, 8] and diffusive [9] problems. As seen above, the brunt of mispredicted $\mathfrak{h}$ is borne by the CFL-number.

53 For cases where $\mathfrak{h}$ is underpredicted, large values of $\mathfrak{C}$ are needed to run close to the stability limit. Conversely, for

54 cases where $\mathfrak{h}$ is overpredicted, $\mathfrak{C}$ needs to be lowered for stability. This is particularly critical for problems utilizing

55 local timestepping (LTS) [10]. In these scenarios, misprediction of $\mathfrak{h}$ in even a small subset of the computational

56 domain can drastically affect overall rate of advancement in time. This is because one needs to lower the value

57 of $\mathfrak{C}$ (which is typically shared over the domain) to satisfy the stability constraint in those cells, thereby reducing

58 the LTS in all other cells much below their actual stable LTS. This has a significant impact on the performance of

59 convergence-acceleration techniques such as *p*-multigrid, where locally-timestepped matrix-free explicit smoothers

60 such as Runge-Kutta (RK) are recommended for their excellent scaling properties at high orders [3]. Therefore,

61 strong variation in $\mathfrak{C}$ is undesirable, as it requires trial-and-error to find its optimum value. Since the exact value of

62 the length-scale depends on the wavenumber of the input signal that is potentially captured by the mesh, it is infea-

63 sible to predict it exactly for complex cases, where the signal is a superposition of several wavenumbers. However,

64 with a reasonable approximate estimation, one can limit the variation of $\mathfrak{C}$ due to wavenumber-superposition to an

65 acceptable range. In typical industrial simulation software it is common to use $\mathfrak{C}$ in the range of 0.1 to 1 for explicit

66 time-integration schemes.

67   How then does one go about estimating a representative length-scale? Since it is connected with the space-

68 component of the discretized system of equations, it must be tied to the computational mesh. In traditional finite-

69 volume (FV) and finite-element (FE) methods for instance, for a problem of dimension $\mathcal{D}$ in space, it is common to

70 estimate $\mathfrak{h}$ as the smallest radius of the $\mathcal{D}$-spheres that inscribe mesh-elements [11]. Another popular measure for

71 FV and FE methods is the ratio of the $\mathcal{D}$-volume and $\mathcal{D}$-semi-area. The overarching idea behind these estimation

72 strategies is finding an appropriate geometric measure that characterizes the shortest discrete length inside each mesh-

73 element. We refer to such a length-scale as geometric length-scale $\mathfrak{h}_g$.

74   High-order (HO) methods such as the discontinuous-Galerkin (DG) method or flux-reconstruction (FR) method

75 represent the solution inside each mesh-element by a piecewise-discontinuous polynomial of order *p*, which is con-

76 stituted by data located at multiple points per element. Across the last three decades, studies have demonstrated the

77 so-called "*p*-dependence of CFL-number" for HO methods, i.e. with increasing *p*, a decrease is observed in the max-

78 imum value of $\mathfrak{C}$ for which the time-integrator is stable [4, 5, 6, 11, 12, 13]. As we have seen earlier, if all quantities

79 are chosen aptly $\mathfrak{C}$ must always approach 1 from the lower limit. The fact that $\mathfrak{C}$ "decreases" with increasing *p* points

80 towards an underestimation of the length-scale $\mathfrak{h}$. Thus, "*p*-dependence of CFL-number" is actually a misnomer for

81 the real issue, which is the *p*-dependence of the length-scale. We refer to this new *p*-dependent length-scale as $\mathfrak{h}_p$.

82 Studies analyzing the *p*-dependence of $\mathfrak{C}$ can be reformulated as the following question: "how to correctly estimate

83 $\mathfrak{h}_p$ as a function of the geometric length-scale $\mathfrak{h}_g$ and p?", i.e.

84
$$\mathfrak{h}_p := \mathfrak{h}_p \left(\mathfrak{h}_g, p\right).$$
(2)

85   Early work on estimating $\mathfrak{h}_p$ for HO-methods was limited to one-dimensional (1D) unsteady linear advection with
86 explicit time-marching. Cockburn and Shu [4] proved formally that, for a p-order spatial DG discretization paried
87 with a k-stage $(k + 1)$-order Runge-Kutta (RK) integrator (where $k = p$), choosing $\mathfrak{h}_p = \mathfrak{h}_g / (2p + 1)$ ensured stability
88 for $p \in [0, 2]$. This estimate was shown to give stable results for higher p in 1D and was within 5% of its actual limit
89 value [5], leading to its widespread usage [7]. For diffusion problems, Gassner et al. [12] proposed scaling $\mathfrak{h}_g$ (whose
90 definition is left open) by a factor of $\beta^* / (2p + 1)^2$, where β^* is yet another scaling factor that varies from 1.5 to 0.13
91 for p ranging from 1 to 5 respectively.

92   In higher spatial dimensions, Toulorge et al. [11] proposed the shortest height of a triangular element as a mea-
93 sure for $\mathfrak{h}_g$ for 2D advection problems. For a given p, this measure generalized well for triangles of varied skewness
94 and across RK-schemes with different stages and orders of accuracy. Nevertheless, the strong dependence of $\mathfrak{C}$ on
95 p remained. In [11], this was characterized as a function of p by curve-fitting. Chalmers and Krivodonova [14]
96 use the cell-width in the direction of the characteristic velocity as the definition of $\mathfrak{h}_g$, and use a scaling-factor of
97 $1/ \left[(2p + 1)\left(1 + 4/ (p + 2)^2\right)\right]$ to compute $\mathfrak{h}_p$ from it. While the predicted timestep is within 5% of the actual max-
98 imum stable timestep, variation in $\mathfrak{C}$ is still more than an order of magnitude between $p = 1$ and $p = 10$. For
99 tensor-product elements (quadrilaterals and hexahedrons), Watkins et al. [15] maximize the non-dimensional convec-
100 tive and diffusive timesteps, subject to the stability constraint of having all eigenvalues of the stability polynomial
101 below 1. To convert these to their physical form (Δt_{con} and Δt_{dif}), they directly use the distances between flux-points
102 on opposite faces as an estimate for $\mathfrak{h}_p$. Finally, their harmonic mean is used to compute the global timestep estimate
103 for the mixed advection-diffusion problem. This is the first study that uses a direct geometric definition of $\mathfrak{h}_p$ instead
104 of scaling $\mathfrak{h}_g$ with a function of p, albeit not exceeding $p = 3$.

105   In summary, we see that most efforts at estimating $\mathfrak{h}_p$ for arbitrary orders and meshes have a common approach:
106 estimate $\mathfrak{h}_g$ using different techniques, and scale it with a factor that is a function of p (and other parameters, such as
107 $\mathcal{D}$). Several procedures have been proposed for each of the two components to fit the predicted $\mathfrak{h}_p$ to yield maximum
108 timesteps for the model problems at hand. However, the methods show large variation in $\mathfrak{C}$. For the few instances
109 where $\mathfrak{h}_p$ is directly computed from the polynomial-discretization of the mesh, it has not been demonstrated to work
110 for $p > 3$. The absence of generality in estimating length-scales has led to alternate approaches to predicting the
111 timestep. Trias and Lehmkuhl [16] estimate the spectral radii of the convective and diffusive operators. However,
112 this is under the condition that the convective operator be skew-symmetric and the diffusive operator be symmetric
113 positive-definite. Loppi et al [10] propose the use of a proportional-integral-derivative (PID) controller based on
114 an estimate of the cell-wise truncation error to control local-timesteps. In our experience the parameters of the
115 PID-controller are sensitive to the quality of the mesh, particularly for direct convergence to steady-state (i.e. not
116 dual time-stepping). Thus, these alternate approaches also have limitations on their generalization. Instead, can the
117 approach of estimating length-scales for HO-methods be made more generalizable?

₁₁₈ Recall that the representative length-scale is tied to the spatial discretization. For HO-methods, this includes
₁₁₉ the mesh-cells as well as the physical location of polynomial-nodes inside them. It is clear from existing methods
₁₂₀ of estimating $\mathfrak{h}_p$ that, for arbitrarily irregular mesh-cells and polynomial-orders, scaling the geometric characteristic
₁₂₁ length $\mathfrak{h}_g$ by a function of p is insufficient in capturing information about the physical location of polynomial-nodes
₁₂₂ in each mesh-cell. In this paper, we attempt to estimate $\mathfrak{h}_p$ directly from the cell-local polynomial-discretization of
₁₂₃ the mesh and flow-quantities. The nature of their relationship is identified through a <u>v</u>on-<u>N</u>eumann <u>a</u>nalysis (VNA)
₁₂₄ framework based on the flux-reconstruction method. The VNA framework supports $2-$ and $3-$dimensional meshes
₁₂₅ with arbitrary skewness and stretching. Using this framework, separate analyses are done for the advection equation
₁₂₆ and the diffusion equation. These result in distinct definitions of length-scales for the advective and diffusive timesteps
₁₂₇ as $\mathfrak{h}_p^{\mathrm{con}}$ and $\mathfrak{h}_p^{\mathrm{dif}}$ respectively. The resulting length-scale estimation strategy greatly reduces the p-dependence of the
₁₂₈ length-scale and scales well for polynomial-orders as high as 10, with minimal influence on $\mathfrak{C}$. It also extends well to
₁₂₉ the density-based <u>R</u>eynolds-<u>a</u>veraged <u>N</u>avier-<u>S</u>tokes (RANS) system of equations.

This paper is organized as follows: Section 2 briefly introduces the flux-reconstruction method. Section 3 is
dedicated to the novel length-scale strategy: first, in Sub-section 3.1 we outline a VNA framework $\mathcal{V}$ using the
flux-reconstruction method on meshes with varying skewness. Given a mesh M with polynomial-order p, and an
input signal of normalized wavenumber $\hat{k}$ at angle θ, $\mathcal{V}$ outputs the maximum stable timestep $\Delta t_{\mathrm{max}\,|\,\mathrm{M},p,\hat{k},\theta}$ for that
configuration. This timestep, together with the characteristic velocity, gives us the ideal length-scale $\mathfrak{h}_{\mathrm{ideal}\,|\,\mathrm{M},p,\hat{k},\theta}$ for
that configuration. By visualizing the variation of $\mathfrak{h}_{\mathrm{ideal}}$ across a number of configurations of M, p, $\hat{k}$ and θ, we uncover
a consistent trend in this variation, which is then be converted into an optimal strategy $\mathcal{S}_{\mathrm{opt}}$. This is done in separate
analyses of the two-dimensional advection-equation (Sub-section 3.2) and diffusion-equation (Sub-section 3.3), from
which we propose a new length-scale estimation strategy with distinct definitions of the convective and diffusive
length-scales. To test the effectiveness of the proposed strategy, we pose the following question in Sub-section 3.4:
"If we use a strategy $\mathcal{S}$ to get $\mathfrak{h}$, and compute the timestep Δt using (1), what max-value of $\mathfrak{C}$ would we need to ensure
that $\Delta t = \Delta t_{\mathrm{max}}$?", i.e.

$$\text{find } \mathfrak{C}_{\mathrm{max}} : \mathfrak{C}_{\mathrm{max}} \frac{\mathfrak{h}}{\|\boldsymbol{\psi}\|} = \Delta t_{\mathrm{max}} \tag{3}$$

₁₃₀ We consider a wide set and types of mesh-skewness, polynomial-orders and flow-physics. The proposed strategy is
₁₃₁ shown to generalize well on a wide variety of meshes and Peclet numbers (Pe) for $p \in [1, 10]$. The Peclet number
₁₃₂ is defined for unit length as the ratio of the convective transport rate and the diffusive transport rate, i.e Pe $= \|\boldsymbol{a}\| / \nu$.
₁₃₃ Generalization to dimension $\mathcal{D} = 3$ is seamless and also demonstrated for representative meshes. Section 4 extends the
₁₃₄ strategy to the compressible Navier-Stokes system of equations, where both the directional information propagation
₁₃₅ by velocity and omni-directional information propagation by the speed-of-sound are accounted for. Its robustness
₁₃₆ on highly skewed meshes is shown through freestream and wall-bounded flow-scenarios and varying flow-physics.
₁₃₇ Finally, in Section 5 we summarize the main findings and propose avenues for future work.

2. Flux reconstruction method

The flux-reconstruction method was first proposed by Huynh [17] as a general formulation that can recover other well-known high-order methods for special choices of the ingredients. Consider the generalized hyperbolic system

$$\partial_t \boldsymbol{U} + \nabla \cdot (\boldsymbol{F}_{\text{ivc}} + \boldsymbol{F}_{\text{vsc}}) = \boldsymbol{S}. \tag{4}$$

The system comprises of $\mathcal{N}$ number of equations. The physical space $\Omega \in \mathbb{R}^{\mathcal{D}}$ is discretized into N_c distinct cells. In each, the discrete solution to (4) is represented by a Lagrange polynomial of order p at $(p+1)^{\mathcal{D}}$ Gauss-solution-points. This solution $\boldsymbol{U}^{\delta} \in \mathbb{R}^{1 \times \mathcal{N}}$ is cell-wise-discontinuous (δ superscript denotes discrete form). Its spatial gradient is represented by $\boldsymbol{Q}^{\delta} \in \mathbb{R}^{\mathcal{D} \times \mathcal{N}}$, and $\boldsymbol{S}^{\delta} \in \mathbb{R}^{1 \times \mathcal{N}}$ represents the source-terms. The flux-reconstruction method constructs a semi-discrete form of (4) as

$$\partial_t \boldsymbol{U} = -\nabla^{\delta} \cdot \left(\mathcal{I}^{p+1}_{\boldsymbol{F}_{\text{ivc}}{}^{\delta\text{C}}} + \mathcal{I}^{p+1}_{\boldsymbol{F}_{\text{vsc}}{}^{\delta\text{C}}} \right) + \boldsymbol{S}^{\delta} \tag{5}$$

where $\mathcal{I}^{p+1}_{\boldsymbol{F}_{\text{ivc}}{}^{\delta\text{C}}}$ and $\mathcal{I}^{p+1}_{\boldsymbol{F}_{\text{vsc}}{}^{\delta\text{C}}}$ are piecewise C^0-continuous inviscid and viscous fluxes respectively. These are constructed from the discontinuous fluxes

$$\begin{aligned}
\boldsymbol{F}_{\text{ivc}}{}^{\delta} &= \boldsymbol{F}_{\text{ivc}} \left(\boldsymbol{U}^{\delta} \right) \\
\boldsymbol{F}_{\text{vsc}}{}^{\delta} &= \boldsymbol{F}_{\text{vsc}} \left(\boldsymbol{U}^{\delta}, \boldsymbol{Q}^{\delta} \right),
\end{aligned} \tag{6}$$

to which corrections are added to ensure that they are continuous at interfaces of cells. At the upper extreme of the cell in reference space, we use as correction-function the left-Radau polynomial of order $p+1$. At the lower extreme of the cell in reference space, we use as correction-function the right-Radau polynomial of order $p+1$. This choice corresponds to the option "g_1" in [17]. These correction-functions apply in all analyses and simulations of this paper. The interface-values for the inviscid flux are calculated using a Riemann solver borrowed from the finite-volume literature, and for the viscous flux using a stabilizing viscous flux resolution method, as

$$\begin{aligned}
\boldsymbol{F}_{\text{ivc}}{}^{\delta\text{I}} &= \mathcal{R}_{\boldsymbol{F}_{\text{ivc}}} \left(\boldsymbol{U}_{-}^{\delta\text{F}}, \boldsymbol{U}_{+}^{\delta\text{F}} \right) \\
\boldsymbol{F}_{\text{vsc}}{}^{\delta\text{I}} &= \mathcal{R}_{\boldsymbol{F}_{\text{vsc}}} \left(\boldsymbol{U}_{-}^{\delta\text{F}}, \boldsymbol{Q}_{-}^{\delta\text{F}}, \boldsymbol{U}_{+}^{\delta\text{F}}, \boldsymbol{Q}_{+}^{\delta\text{F}} \right),
\end{aligned} \tag{7}$$

where $\boldsymbol{U}_{-}^{\delta\text{F}}$ and $\boldsymbol{U}_{+}^{\delta\text{F}}$ are the discontinuous solution-values interpolated to the interface from the left and right respectively. Likewise, $\boldsymbol{Q}_{-}^{\delta\text{F}}$ and $\boldsymbol{Q}_{+}^{\delta\text{F}}$ are the interpolated discontinuous corrected gradients. Without loss of generality, we use the Roe solver for the inviscid flux and the local discontinuous-Galerkin (LDG) flux [18] for the viscous flux. For a detailed description, the reader is referred to [19].

We advance (5) in time using a 3rd-order Runge-Kutta (RK33) scheme [20, 21], the details of which are described in Appendix A. For acceleration to steady state or pseudo steady state, a local timestep is computed for each cell in the mesh by taking the minimum of the convective and diffusive timesteps (described later in (21) and (23)) in that cell. For time-accurate fully-explicit simulations, the global timestep is calculated as the minimum of the local-timesteps.

3. Length-scale estimation

The ideal explicit timestep Δt_{ideal} should be selected such that the ratio of the maximum stable timestep Δt_{max} with Δt_{ideal} equals 1, i.e.

$$\frac{\Delta t_{\text{max}}}{\Delta t_{\text{ideal}}} = 1. \tag{8}$$

Δt_{ideal} is the ratio of a representative length-scale $\mathfrak{h}_{\text{ideal}}$ and the physical rate of information propagation of the problem $\|\boldsymbol{\psi}\|$, as [4, 5, 6, 7, 8]:

$$\Delta t_{\text{ideal}} = \frac{\mathfrak{h}_{\text{ideal}}}{\|\boldsymbol{\psi}\|}. \tag{9}$$

$\|\boldsymbol{\psi}\|$ depends on the problem at hand. For example, for convection it is the characteristic velocity $\|\boldsymbol{a}\|$, and for diffusion it is the kinematic viscosity per unit characteristic length $\nu/\mathfrak{h}$. Substituting (9) in (8), we obtain the following form of the stability-limit:

$$\frac{\Delta t_{\text{max}} \|\boldsymbol{\psi}\|}{\mathfrak{h}_{\text{ideal}}} = 1, \tag{10}$$

i.e. *if* the ideal representative length-scale is known, then the estimated timestep will be ideal and equal to the maximum stable timestep Δt_{max}. However, $\mathfrak{h}_{\text{ideal}}$ is typically not known, and is not trivial to estimate. Instead, one might find an approximate length-scale $\mathfrak{h}$ which might or might not be close to $\mathfrak{h}_{\text{ideal}}$. Using this length-scale, the approximated timestep is now $\Delta t_{\text{approx}} = \frac{\mathfrak{h}}{\|\boldsymbol{\psi}\|}$. The ratio of Δt_{max} with Δt_{approx} is no longer assured to be equal to 1 but rather to a constant $\mathfrak{C}_{\text{exact}}$, i.e.

$$\frac{\Delta t_{\text{max}} \|\boldsymbol{\psi}\|}{\mathfrak{h}} = \mathfrak{C}_{\text{exact}}, \tag{11}$$

or, in other words,

$$\Delta t_{\text{max}} = \mathfrak{C}_{\text{exact}} \frac{\mathfrak{h}}{\|\boldsymbol{\psi}\|}. \tag{12}$$

In reality, one knows neither Δt_{max} nor $\mathfrak{C}_{\text{exact}}$ - only the rate of physical information propagation $\|\boldsymbol{\psi}\|$ and the approximate length-scale $\mathfrak{h}$ are known. The usual process is to *guess* a value $\mathfrak{C}$, and with it compute the timestep as

$$\Delta t = \mathfrak{C} \frac{\mathfrak{h}}{\|\boldsymbol{\psi}\|}. \tag{13}$$

If the simulation fails, then one knows that $\Delta t > \Delta t_{\text{max}}$, meaning that $\mathfrak{C} > \mathfrak{C}_{\text{exact}}$. Thus, one lowers $\mathfrak{C}$, recomputes Δt using (13) and re-runs the simulation. This process is repeated until stability is achieved. Note that choosing an arbitrarily low value of $\mathfrak{C}$ might guarantee stability, but leads to extremely slow advancement in time as $\Delta t \ll \Delta t_{\text{max}}$. Therefore, one tries to estimate $\mathfrak{C} \approx \mathfrak{C}_{\text{exact}}$ to obtain $\Delta t \approx \Delta t_{\text{max}}$.

This trial-and-error process to seek $\mathfrak{C} \approx \mathfrak{C}_{\text{exact}}$ masks a more fundamental problem: the deviation of $\mathfrak{h}$ from $\mathfrak{h}_{\text{ideal}}$. To see this, note that if $\mathfrak{h} \to \mathfrak{h}_{\text{ideal}}$ in (11), then using (10) we see that $\mathfrak{C}_{\text{exact}} \to 1$ and we seek $\mathfrak{C} \approx 1$. That is, if the value of the approximate length-scale $\mathfrak{h}$ is close to the ideal length-scale $\mathfrak{h}_{\text{ideal}}$, then we can use a value of $\mathfrak{C}$ close to 1 independent of the problem at hand. As discussed before, existing methodologies are unable to do this for meshes of arbitrary skewness. Our goal is to find a length-scale definition that takes into account both the geometric and polynomial discretization. To extract patterns of the variation of this length-scale with mesh-skewness, p, etc., we

		TT		
	LT	T	RT	
LL	L	O	R	RR
	LB	B	RB	
		BB		

		TTt TTl TTr TTb		
	LTt LTl LTr LTb	Tt Tl Tr Tb	RTt RTl RTr RTb	
LLt LLl LLr LLb	Lt Ll Lr Lb	Ot Ol Or Ob	Rt Rl Rr Rb	RRt RRl RRr RRb
	LBt LBl LBr LBb	Bt Bl Br Bb	RBt RBl RBr RBb	
		BBt BBl BBr BBb		

Fig. 1: Labeling for cells (top) and cell-faces (bottom) of the 5×5 meshes used in the two-dimensional VNA.

will assemble a VNA framework on skewed meshes (see Figure 2 for examples of the skewed meshes) for the $\mathcal{D} = 2$ linear advection-diffusion equation

$$\partial_t u + \nabla \cdot (\boldsymbol{F} + \boldsymbol{G}) = 0, \tag{14}$$

$$\nabla = \begin{bmatrix} \partial_{x_1} & \partial_{x_2} \end{bmatrix} \ , \ \boldsymbol{F} = u \begin{bmatrix} a \\ b \end{bmatrix} \ , \ \boldsymbol{G} = \nu \begin{bmatrix} -\partial_{x_1} u \\ -\partial_{x_2} u \end{bmatrix}.$$

VNA has been successfully employed in the past for the dispersion-dissipation analysis [22, 23, 24] and stability-analysis [6, 25] of high-order methods.

3.1. Two-dimensional von-Neumann analysis framework on skewed meshes

We consider a 5×5 mesh composed of quadrilateral cells. The element being analysed is the central cell C_O. The neighbors of C_O to its left, right, bottom and top are C_L, C_R, C_B and C_T respectively. Cells further on in each direction are denoted by C_{LL}, C_{RR}, C_{BB} and C_{TT}. The diagonal point-neighbours of C_O are C_{LB}, C_{LT}, C_{RB} and C_{RT}. Data belonging to a given cell is represented by a subscript, e.g. $(\cdot)_O$ for C_O. For a given cell, data at the left, right, bottom and top faces is denoted by subscripts of l, r, b and t respectively (see Figure 1 for details). Unit-normals at flux-points are denoted by $\bar{\boldsymbol{n}}$ and are assumed to go from left-to-right, bottom-to-top.

The assembly of the VNA framework is detailed in Appendix B, and results in the following semi-discrete equation

$$\begin{aligned} \partial_t u = {} & \mathfrak{P}_O u_O{}^{\delta D} + \mathfrak{P}_L u_L{}^{\delta D} + \mathfrak{P}_R u_R{}^{\delta D} + \mathfrak{P}_B u_B{}^{\delta D} + \mathfrak{P}_T u_T{}^{\delta D} \\ & + \mathfrak{P}_{LL} u_{LL}{}^{\delta D} + \mathfrak{P}_{RR} u_{RR}{}^{\delta D} + \mathfrak{P}_{BB} u_{BB}{}^{\delta D} + \mathfrak{P}_{TT} u_{TT}{}^{\delta D} \\ & + \mathfrak{P}_{LB} u_{LB}{}^{\delta D} + \mathfrak{P}_{LT} u_{LT}{}^{\delta D} + \mathfrak{P}_{RB} u_{RB}{}^{\delta D} + \mathfrak{P}_{RT} u_{RT}{}^{\delta D}, \end{aligned} \tag{15}$$

where the $\mathfrak{P}_i$ matrix contains all operations applied on the discontinuous solution $u_i{}^{\delta D}$ in cell C_i. We impose initial solutions of the form

$$u (x_1, x_2) = \exp\left(i\hat{k} \left(x_1 \cos\theta + x_2 \sin\theta\right)\right), \tag{16}$$
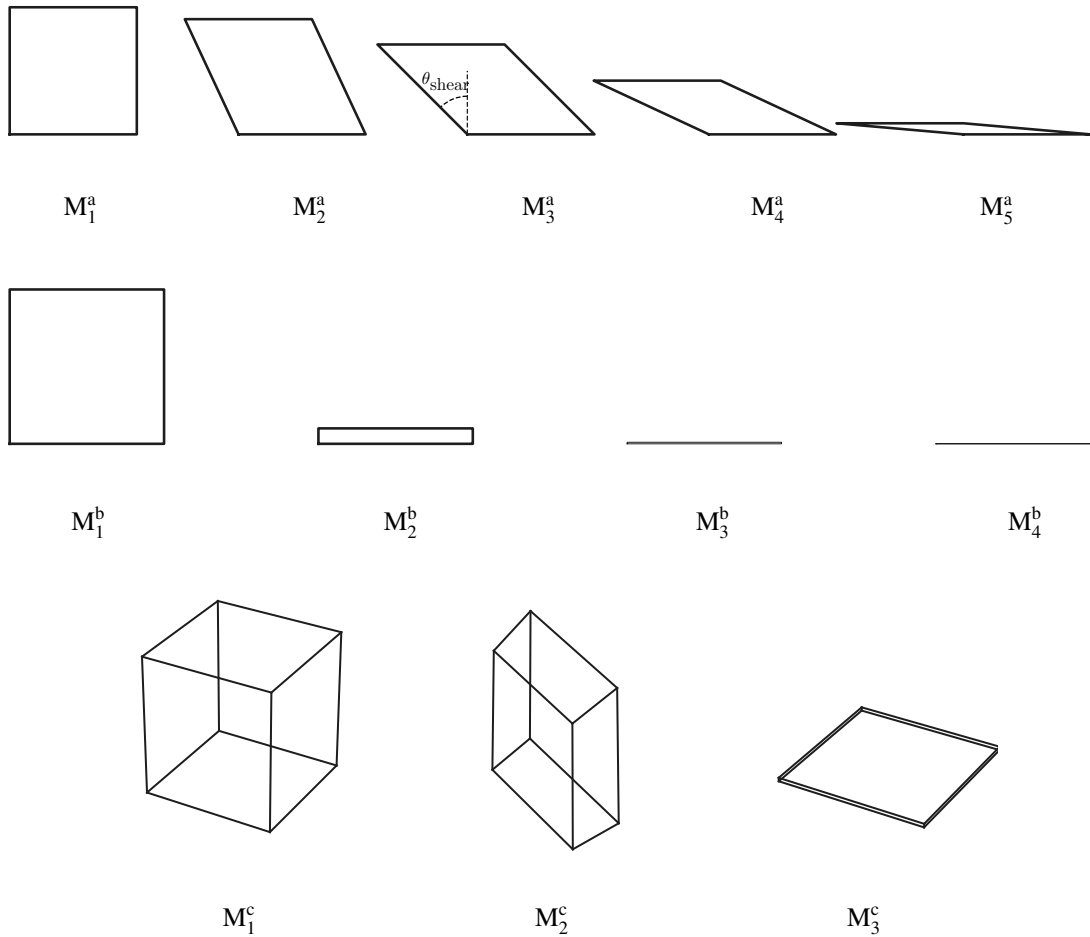
Fig. 2: Meshes used in assessing the robustness of the proposed length-scale strategy through VNA. (top) Progressively sheared quad-meshes with shear-angles 0° (M_1^a), 25° (M_2^a), 45° (M_3^a), 65° (M_4^a) and 85° (M_5^a) respectively. Meshes M_1^a and M_4^a are used for the analyses of Sub-section 3.2 and Sub-section 3.3. (middle) Meshes with increasing aspect-ratios 1 (M_1^b), 10 (M_2^b), 100 (M_3^b) and 1000 (M_4^b). (bottom) Meshes used in the three-dimensional VNA. Each 2D-mesh contains 5×5 identical cells ($5 \times 5 \times 5$ in 3D) that have been hidden for clarity of shape.

.

198 where $\hat{k}$ is the normalized wavenumber and θ is the angle of incidence of the initial solution wave to the horizontal

199 axis. This allows us to express the initial solution u_j in any cell C_j as a function of the initial solution u_O in cell C_O as

$$u_j = u_O \exp\left(i\hat{k}\left(\left(x_{1,j} - x_{1,O}\right)\cos\theta + \left(x_{2,j} - x_{2,O}\right)\sin\theta\right)\right). \tag{17}$$

201 Writing all discontinuous discrete solutions in (15) in terms of $u_O^{\delta D}$ and aggregating the resulting matrices into

202 $\mathfrak{P}$, the semi-discrete form reduces to

$$\partial_t u = \mathfrak{P} u_O^{\delta D}. \tag{18}$$

204 (18) can be converted into a solution-update equation by applying a time-discretization (for instance, the RK33 scheme

205 as in [6]) with some timestep Δt as

$$u_O^{\delta D,n+1} = R u_O^{\delta D,n}$$

$$R = I + \frac{\Delta t \mathfrak{P}}{1!} + \frac{(\Delta t \mathfrak{P})^2}{2!} + \frac{(\Delta t \mathfrak{P})^3}{3!}. \tag{19}$$

208 For a stable update of the solution, the spectral-radius of R must be less than or equal to 1 [26]. The timestep that

209 fulfils this condition is referred to as $\Delta t_{\max}$, i.e.

$$\Delta t_{\max} := \max(\Delta t) \mid \sigma\left(R(\Delta t)\right) < 1 \tag{20}$$

211 where $\sigma\left(\cdot\right)$ represents the spectral radius.

212 *3.2. Convective time-step trends*

In this subsection, we use the VNA framework to identify the variation-trends of the maximum convective time-step using pure advection. We are interested in observing the variation of the length-scale $\mathfrak{h}$ with the maximum stable timestep $\Delta t_{\max}$ (obtained from (20)) that keeps the CFL-number at or below 1. Typically, the convective timestep is computed as

$$\Delta t_{\mathrm{con}} = \mathfrak{C} \frac{\mathfrak{h}}{\|\boldsymbol{a}\|}. \tag{21}$$

213 Rewriting and setting $\mathfrak{C} = 1$ and $\Delta t_{\mathrm{con}} = \Delta t_{\max}$,

$$\mathfrak{h} = \Delta t_{\max} \|\boldsymbol{a}\| = \Delta t_{\max} \sqrt{a^2 + b^2}, \tag{22}$$

215 where a and b are the advection velocity components in the x_1 and x_2 coordinate-directions. These trends will uncover

216 the definition of the convective length-scale $\mathfrak{h}_p^{\mathrm{con}}$ that keeps the change in $\mathfrak{C}$ to a minimum. Pure advection is simulated

217 for all angles of incidence, i.e. $\nu = 0$, $\theta \in [0, \pi]$. The advection velocity components are therefore $a = \cos\theta$, $b =$

218 $\sin\theta$. The effect of the polynomial-order is analyzed by studing a range of polynomial-orders $p \in [1, 5]$. Two 5×5

219 grids are analyzed: M_1^a: a uniform, square grid, and M_4^a: a uniform left-leaning parallelogram grid that makes an angle

220 of $65°$ with the negative x_1 axis (see Figure 2).
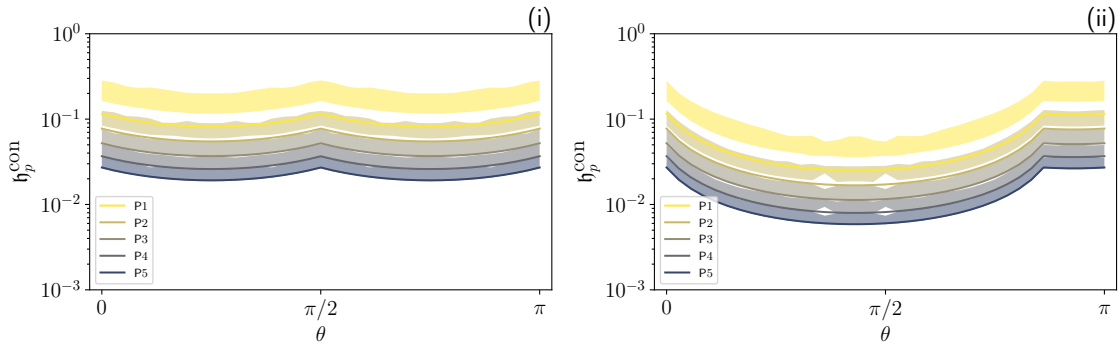
221 The trend is uncovered through Figure 3:

Fig. 3: Variation of optimum convective length-scale $\mathfrak{h}_p^{con}$ with angle of incidence θ for range of p (lower to higher: blue to yellow) on (i) uniform square mesh M_1^a and (ii) skewed parallelogram mesh M_4^a. Bands indicate variation with respect to $\hat{k}$. Solid lines plot the shortest flow-direction-distance of solution-points to sub-cell diagonals (see Figure 4). These results correspond to Sub-section 3.2 and Table 1.
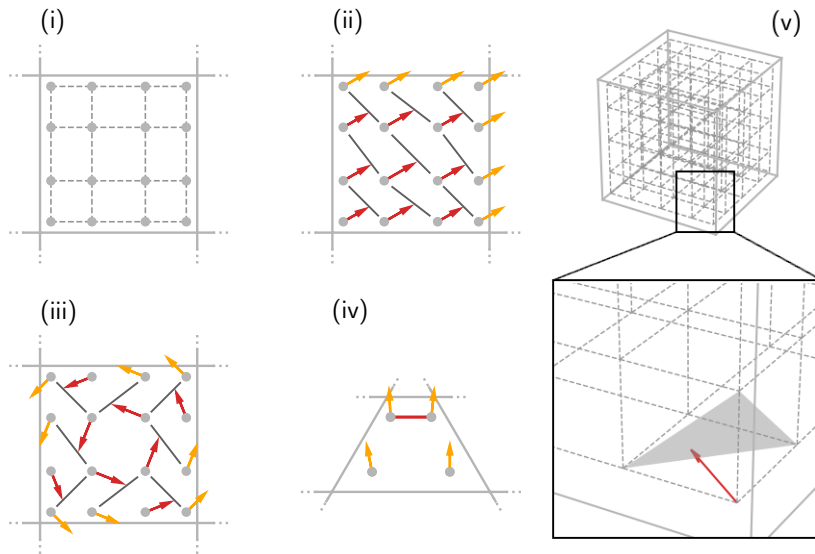

Fig. 4: (i) Schematic of sub-cells (dashed lines) in a mesh cell with $p = 3$. (ii) Schematic of distances in flow-direction to sub-cell diagonal for uniform flow-direction at $\theta = \pi/6$. Red arrows are candidates for length-scale (the smallest of these is chosen as $\mathfrak{h}_p^{con}$ for this cell). Yellow arrows do not participate. (iii) Similar schematic for flow with pointwise differing flow-direction. (iv) For cases where none of the solution-points contains a candidate length, $\mathfrak{h}_p^{con}$ is assigned the minimum distance between solution-points. (v) $\mathcal{D} = 3$ schematic of sub-cells. Inset shows an example of sub-cell diagonal-plane and its use in calculating the convective length-scale candidate for a solution-point and flow-direction.

Table 1: Ratio of theoretical convective length-scale that keeps CFL number at or below 1 (i.e. $\mathfrak{h}$ from (22)) and the shortest flow-direction-distance of solution-points to sub-cell-diagonals (i.e. $\mathfrak{h}_p^{con}$). Rows indicate polynomial orders, columns indicate minimum, maximum and mean values across $\hat{k}$ and θ for meshes M_1^a and M_4^a. These results correspond to Sub-section 3.2 and Figure 3.

	M_1^a			M_4^a		
	min	mean	max	min	mean	max
$P1$	1.4	1.8	2.6	1.4	1.8	2.6
$P2$	1.1	1.3	1.7	1.1	1.3	1.7
$P3$	1.0	1.2	1.5	1.0	1.2	1.5
$P4$	0.97	1.1	1.4	0.98	1.1	1.4
$P5$	0.97	1.1	1.4	0.97	1.1	1.4

- From the VNA, we obtain the maximum stable timestep for a given choice of p, $\hat{k}$ and θ. We then assume a CFL number of 1, and back-calculate the length-scale needed to obtain this maximum stable timestep. All values of this length-scale for different choices of p, $\hat{k}$ and θ are plotted as colored bands in Figure 3. The color of the band indicates the value of p, while the width of the band indicates the variation of the length-scale with respect to $\hat{k}$. Note how the length-scale range varies with the angle of incidence θ. We are interested in finding out a definition of the length-scale that can capture this variation with p and θ.

- In solid lines, we plot the minimum distance in the flow direction between any solution-point and its opposite sub-cell diagonal. For a schematic of this distance see Figure 4-(ii). Sub-cells are formed by connecting the solution-points in a regular grid in reference-space and transforming that grid into physical space. See Figure 4-(i) for a schematic of sub-cells for $\mathcal{D} = 2$, and Figure 4-(v) for $\mathcal{D} = 3$. Flow-directions that do not intersect their corresponding sub-cell diagonals are excluded from the computation.

- On closer inspection, we see that this distance correlates well with the variation we wish to capture. This is observed both for results on both the square-mesh and shear-skewed mesh, as seen in Figure 3-(i) and Figure 3-(ii) respectively. Table 1 shows the minimum, maximum and mean values of the ratio between the theoretical and predicted length-scales. We see that the mean value of this ratio tends towards 1.

The definition extends seamlessly to $\mathcal{D} = 3$. Here, the length-scale is the minimum distance in the flow direction between any solution-point and its corresponding sub-cell diagonal-plane. This diagonal-plane is constructed by connecting the adjacent sub-cell-points (see the inset of Figure 4-(v) for an example). Note that, if we collapse the $\mathcal{D} = 3$ case to $\mathcal{D} = 2$ along any direction, we recover the $\mathcal{D} = 2$ length-scale definition.

We choose this definition as our definition of the convective length-scale $\mathfrak{h}_p^{con}$. We henceforth refer to this strategy as "GD1" (i.e. we consider the geometry of the mesh-discretization and the directional-geometry of the polynomial-

discretization). In the rare event that GD1 does not produce any candidates (see Figure 4-(iv)), the shortest distance between solution-points of that cell is chosen as $\mathfrak{h}_p^{\text{con}}$; note that this case can only occur for $p = 1$.

3.3. Diffusive time-step trends

We conduct a similar exercise as in Sub-section 3.2 to identify variation-trends in the maximum diffusive time-step, now using pure diffusion. We are interested in observing the variation of the length-scale $\mathfrak{h}$ with the maximum stable timestep Δt_{max} (obtained from (20)) that keeps the CFL-number at or below 1. The diffusive timestep is typically computed as

$$\Delta t_{\text{dif}} = \mathfrak{C}\frac{\mathfrak{h}^2}{\nu}. \tag{23}$$

Rewriting and setting $\mathfrak{C} = 1$ and $\Delta t_{\text{dif}} = \Delta t_{\text{max}}$,

$$\mathfrak{h} = \sqrt{\Delta t_{\text{max}}\nu}. \tag{24}$$

These trends will uncover the definition of the diffusive length-scale $\mathfrak{h}_p^{\text{dif}}$ that keeps the change in $\mathfrak{C}$ to a minimum. Meshes M_1^a and M_4^a are used. Convection is absent; thus $a = 0$, $b = 0$. Kinematic viscosity $\nu = 1$ is used. The parameters of the LDG viscous flux are chosen as $\beta = 0.5$, $\tau = 0.1$.

Figure 5 shows the variation of maximum $\mathfrak{h}$ (calculated using (24)) for different p at varying θ. For fixed p and θ, the variation with $\hat{k}$ is encapsulated by the upper and lower bounds of the corresponding colored band. For both meshes, the change with respect to θ is negligible, which is reasonable as diffusion is omnidirectional. This property also points towards choosing the shortest discrete distance as the diffusive length-scale. For a given mesh-cell and polynomial discretization, this distance is the shortest distance between any solution-point and the cell-boundary. This distance is plotted as solid-lines in Figure 5 for both meshes, and shows good correlation with the maximum length-scale that yields a stable time-step. Table 2 shows the minimum, maximum and mean values of the ratio between the theoretical and predicted length-scales. We see that the mean value of this ratio tends towards 1. We therefore

Table 2: Ratio of theoretical diffusive length-scale that keeps CFL number at or below 1 (i.e. $\mathfrak{h}$ from (24)) and the shortest distance between solution-points and cell-boundary (i.e. $\mathfrak{h}_p^{\text{dif}}$). Rows indicate polynomial orders, columns indicate minimum, maximum and mean values across $\hat{k}$ and θ for meshes M_1^a and M_4^a. These results correspond to Sub-section 3.3 and Figure 5.

	M_1^a			M_4^a		
	min	mean	max	min	mean	max
$P1$	1.2	1.5	1.7	1.1	1.2	1.3
$P2$	0.91	1.3	1.6	0.89	1.2	1.4
$P3$	0.92	1.2	1.4	0.58	0.84	1.1
$P4$	1.00	1.3	1.5	0.78	1.1	1.3
$P5$	0.83	1.1	1.4	0.78	0.95	1.1
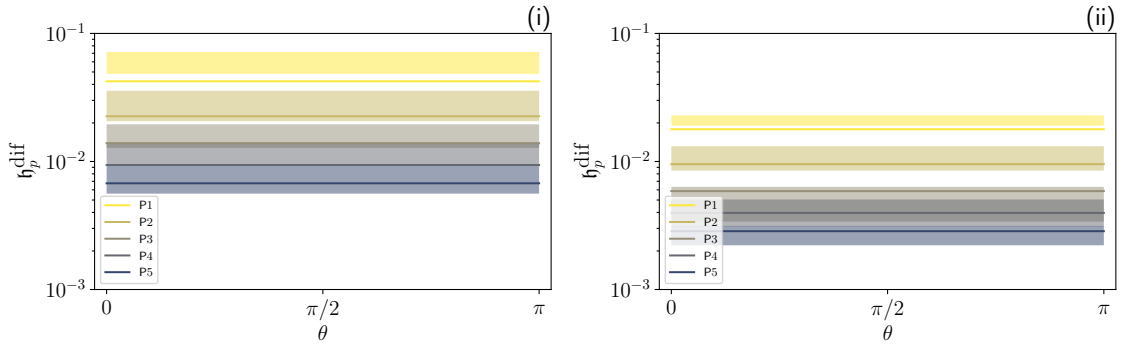
Fig. 5: Variation of optimum diffusive length-scale $\mathfrak{h}_p^{\mathrm{dif}}$ with initial solution orientation angle θ for range of p (lower to higher: blue to yellow) on (i) uniform square mesh $\mathrm{M}_1^{\mathrm{a}}$ and (ii) skewed parallelogram mesh $\mathrm{M}_4^{\mathrm{a}}$. Bands indicate variation with respect to $\hat{k}$. Solid lines plot the shortest distance between solution-points and cell-boundary. These results correspond to Sub-section 3.3 and Table 2.

choose this as the definition of the diffusive length scale $\mathfrak{h}_p^{\mathrm{dif}}$. This strategy is henceforth referred to as "GG1" (i.e. we consider the geometry of the mesh-discretization and the geometry of the polynomial-discretization).

3.4. Length-scale definition tests

Having proposed an optimal strategy, in this section we test its effectiveness by posing the following question: "If we use a given strategy to get $\mathfrak{h}$, and use it to compute the timestep Δt, what max-value of $\mathfrak{C}$ would we need to ensure that $\Delta t = \Delta t_{\mathrm{max}}$?", i.e.

$$\text{find } \mathfrak{C}_{\mathrm{max}} : \mathfrak{C}_{\mathrm{max}} \cdot \min\left(\frac{\mathfrak{h}_p^{\mathrm{con}}}{\|\boldsymbol{a}\|} \quad , \quad \frac{\left(\mathfrak{h}_p^{\mathrm{dif}}\right)^2}{\nu} \right) = \Delta t_{\mathrm{max}} \tag{25}$$

The tests are done on a range of meshes with varying mesh-skewness, polynomial-orders ranging from 1 to 10 and Peclet numbers (Pe) ranging from 0 to ∞. Note that this includes tests for pure convection (Pe = ∞) and pure diffusion (Pe = 0). The tests are performed in the VNA framework for $\theta \in [0, \pi]$ and $\hat{k} \in [0, 2\pi]$. For each configuration of the set $\{\text{mesh, length-scale strategy}, p, \text{Pe}, \hat{k}, \theta\}$ we obtain the maximum stable timestep Δt_{max} using (20) and subsequently the maximum stable CFL as

$$\mathfrak{C}_{\mathrm{max}} = \max\left(\frac{\|\boldsymbol{a}\| \, \Delta t_{\mathrm{max}}}{\mathfrak{h}_p^{\mathrm{con}}} \quad , \quad \frac{\nu \Delta t_{\mathrm{max}}}{\left(\mathfrak{h}_p^{\mathrm{dif}}\right)^2} \right), \tag{26}$$

where $\boldsymbol{a}$ is the advection-speed vector. The smaller the variation in the value of $\mathfrak{C}_{\mathrm{max}}$ across all configurations, the better is the strategy. The reason we focus on the CFL number $\mathfrak{C}$ is because it is $\mathfrak{C}$ that is exposed as a parameter to the user. As we have seen in the introduction, having $\mathfrak{C}$-variation limited between 0.1 and 1 is equvalent to having a Δt close to Δt_{max}.

The length-scale strategies that are studied are:

- GD1-GG1: This is a combination of the convective and diffusive length-scale strategies derived in Sub-section 3.2 and Sub-section 3.3. We use GD1 as the estimate for $\mathfrak{h}_p^{\mathrm{con}}$ and GG1 as the estimate for $\mathfrak{h}_p^{\mathrm{dif}}$. This strategy is described in a schematic in Figure 6.
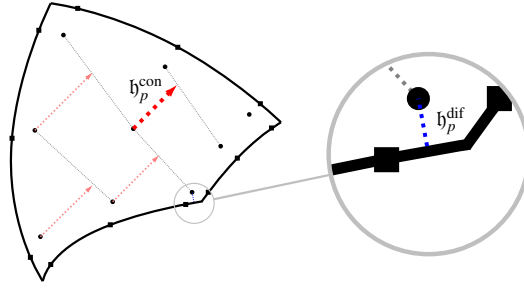
Fig. 6: Schematic describing the cell-local length-scale calculation strategy GD1-GG1 used in this paper, here demonstrated for a $p = 2$ Gauss-point discretization on an arbitrary curved quadrilateral cell. The convective length-scale $\mathfrak{h}_p^{\text{con}}$ is computed as the shortest directional-distance between any solution-point and its corresponding sub-cell-diagonal (dotted red line). The diffusive length-scale $\mathfrak{h}_p^{\text{dif}}$ is computed as the normal distance between any solution-point and the nearest cell-wall (dotted blue line).

- GS1: This strategy is a popular choice in the HO-community [4, 5, 7] - it involves computing an estimate of the geometric length-scale of the cell ($\mathfrak{h}_g$), and then scaling it by the factor $1/(2p + 1)$ to account for the polynomial-order. The geometric length-scale for quad-cells is estimated as the ratio of its area and semi-perimeter. The resulting length-scale estimate is used for both $\mathfrak{h}_p^{\text{con}}$ and $\mathfrak{h}_p^{\text{dif}}$. "GS1" therefore refers to considering the geometry of the mesh-discretization and scaling it with a function of the polynomial-order.

- GS2: Mostly used for diffusion-dominated flows [7, 12], this strategy also computes $\mathfrak{h}_g$ similar to GS1, but scales it with the factor $1/p^2$. Again, the resulting length-scale estimate is used for both $\mathfrak{h}_p^{\text{con}}$ and $\mathfrak{h}_p^{\text{dif}}$. "GS2" therefore refers to considering the geometry of the mesh-discretization and scaling it with another function of the polynomial-order.

- GG2: The final strategy studied here computes estimates both $\mathfrak{h}_p^{\text{con}}$ and $\mathfrak{h}_p^{\text{dif}}$ as the shortest distance between the solution-points of the cell [8, 27]. Similar to GD1-GG1, this strategy takes into account the geometric and polynomial discretization, rather than using the scaling approach of GS1 and GS2.

3.4.1. Effect of shear-skewness

The first study introduces skewness in the mesh by shearing a square-mesh into a progressively sharper paral-lelogram shape as shown in Figure 2. This allows us to investigate the robustness of the length-scale strategy on non-cartesian and highly distorted cells.

Results are presented in Figure 7, with a quantitative summary in Table 3. The first observation is that the proposed strategy GD1-GG1 shows minimal variation of $\mathfrak{C}$ across all meshes, p, $\hat{k}$ and θ, particularly at higher Pe. For instance at Pe $= \infty$, $\mathfrak{C}$-variation is limited between 1.3 and 0.2 with GD1-GG1, whereas for all other strategies it varies by two orders of magnitude. This points to the effectiveness of GD1-GG1 in capturing the directional dependence of Δt_{max}. This is especially true for meshes with high skewness, where Δt_{max} can vary significantly depending on the orientation of flow-direction with respect to the mesh-skewness. If the flow-direction is aligned closer to the long-diagonal of

Table 3: Minimum, average and maximum values of $\mathfrak{C}_{\max}$ with different length-scale strategies at varying Pe on **shear-skewed meshes** (see Sub-section 3.4.1 and Figure 7). Each set of minimum-mean-maximum values encapsulates variation with respect to p, $\hat{k}$ and θ.

Pe:	0			10^{-3}			1			10^3			∞		
	min	mean	max	min	mean	max	min	mean	max	min	mean	max	min	mean	max
GD1-GG1	0.06	0.28	0.72	0.27	0.43	0.8	0.27	0.45	1.3	0.18	0.41	1.3	0.21	0.61	1.3
GS1	0.01	0.21	1.2	0.06	0.32	1.3	0.05	0.35	2.1	0.05	1.1	9.9	0.37	2.4	49
GS2	0.05	0.68	2.0	0.07	1.1	2.1	0.07	1.1	2.1	0.32	1.7	5.2	0.42	4.9	68
GG2	0.003	0.019	0.096	0.01	0.03	0.11	0.02	0.03	0.17	0.02	0.32	2.8	0.2	0.79	14

Table 4: Minimum, average and maximum values of $\mathfrak{C}_{\max}$ with different length-scale strategies at varying Pe on **meshes with high-aspect-ratio cells** (see Sub-section 3.4.2 and Figure 8). Each set of minimum-mean-maximum values encapsulates variation with respect to p, $\hat{k}$ and θ.

Pe:	0			10^{-3}			1			10^3			∞		
	min	mean	max	min	mean	max	min	mean	max	min	mean	max	min	mean	max
GD1-GG1	0.11	0.6	1.5	0.21	0.97	1.6	0.44	0.98	2.4	0.25	0.89	1.6	0.07	0.59	1.3
GS1	0.008	0.17	1.2	0.011	0.27	1.3	0.047	0.27	2.1	0.047	0.53	4.2	0.079	95	3800
GS2	0.013	0.56	2.0	0.07	0.89	2.1	0.07	0.89	2.1	0.068	1.1	3.6	0.38	65	2300
GG2	0.007	0.045	0.21	0.012	0.073	0.21	0.025	0.073	0.32	0.046	0.21	2.3	0.082	65	2300

the cell, a greater $\Delta t_{\max}$ can be afforded. However, the older strategies always make a conservative prediction of the length-scale, leading to very high values of $\mathfrak{C}$ that yield $\Delta t_{\max}$. On the other hand, if the flow-direction is aligned closer to the short-diagonal, $\Delta t_{\max}$ will be much smaller. This effect is more pronounced with cells that are highly skewed. For diffusion-dominated cases (Pe $\ll$ 1) also, GD1-GG1 generalizes better across p than the other strategies.

3.4.2. Effect of high-aspect-ratios

The second study analyzes the effectiveness of the proposed length-scale strategy on meshes that contain cells with high-aspect-ratios. Such cells are common in CFD, especially in the boundary-layer and wake. A series of four meshes is studied, with aspect-ratios 1, 10, 100 and 1000 respectively (see Figure 2). Results are presented in Figure 8, with a quantitative summary in Table 4. Again, GD1-GG1 generalizes very well across all values Pe and p, providing optimal $\mathfrak{C}$-values between the range of 0.1 and 1. In contrast, the other strategies show $\mathfrak{C}$-variation of more than three orders of magnitude, especially at high Pe. This can be explained with a similar reasoning as for Sub-section 3.4.1: $\Delta t_{\max}$ is greater when the flow is aligned in the direction of elongation. The GD1-GG1 strategy accounts for this change, and is hence able to keep the $\mathfrak{C}$-variation in check. Conversely, the conservative estimate of the other strategies proves too restrictive higher aspect ratios. Thus, a much greater $\mathfrak{C}$ is required to yield $\Delta t_{\max}$.
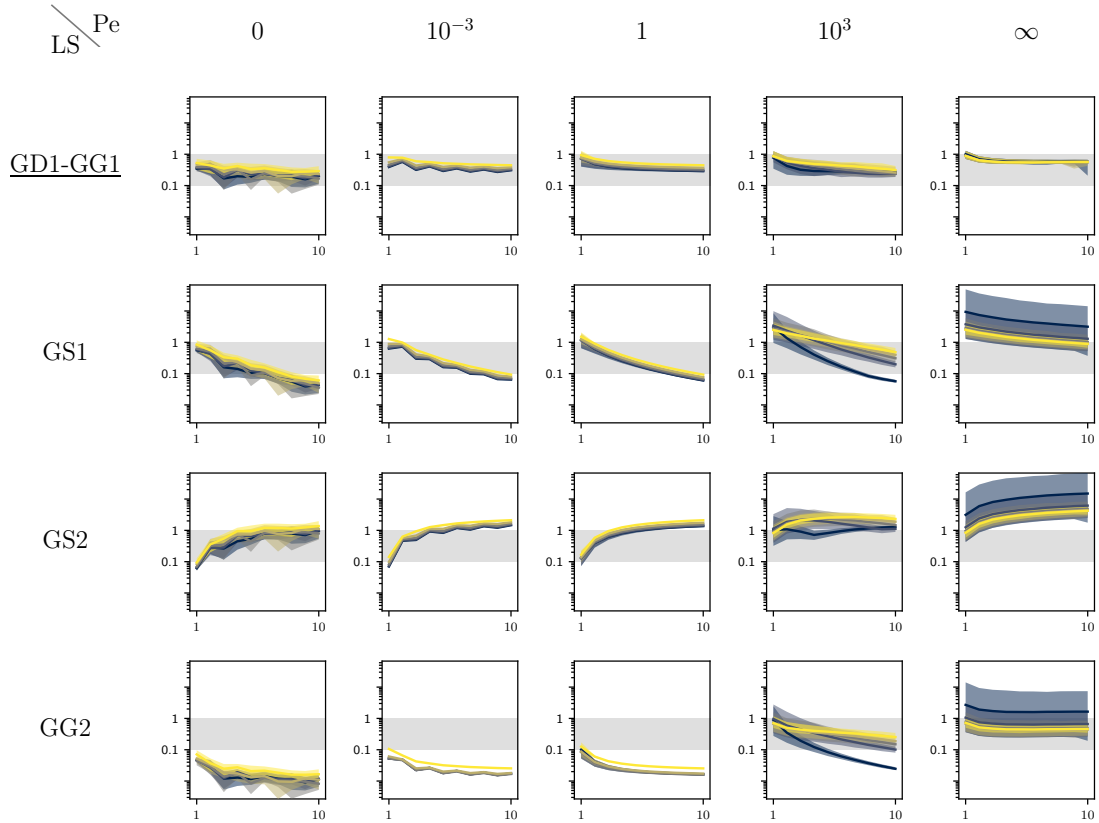
Fig. 7: Results of VNA on **shear-skewed meshes** (see Sub-section 3.4.1 and Table 3). Maximum CFL number $\mathfrak{C}_{max}$ in log-scale (ordinate of each sub-plot) plotted against increasing polynomial-orders $p \in [1, 10]$ (abscissa of each sub-plot). All sub-plots share the same limits on the axes. The grey-shaded area marks the region of $\mathfrak{C} \in [0.1, 1]$, which is a practically reasonable range. Colors represent meshes (Figure 2) going from less skewed (yellow) to more skewed (blue). Color-shaded areas depict variation of $\mathfrak{C}$ with $\hat{k}$ and θ, while color-lines plot the average values of $\mathfrak{C}$. Plot-rows indicate length-scale strategies and plot-columns vary the Peclet number Pe. For details on construction of the sub-figures, see Appendix C.
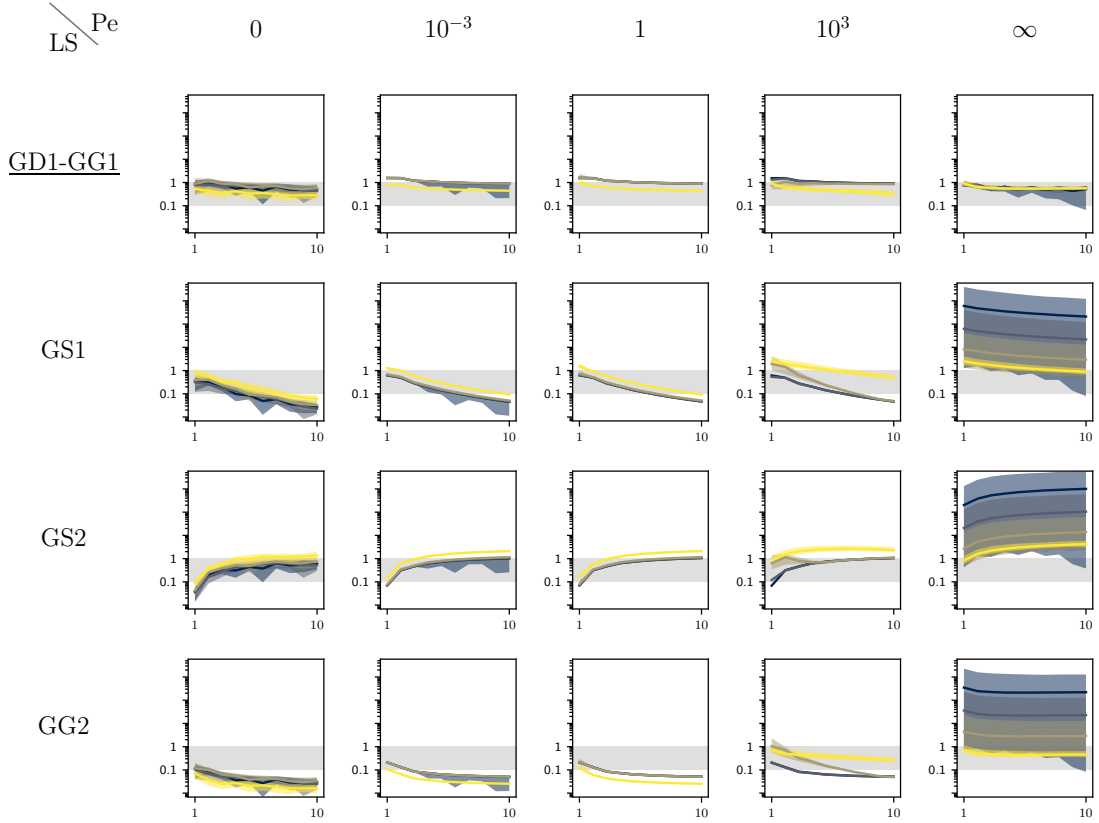
Fig. 8: Results of VNA on **meshes with high-aspect-ratio cells** (see Sub-section 3.4.2 and Table 4). Maximum CFL number $\mathfrak{C}_{max}$ in log-scale (ordinate of each sub-plot) plotted against increasing polynomial-orders $p \in [1, 10]$ (abscissa of each sub-plot). All sub-plots share the same limits on the axes. The grey-shaded area marks the region of $\mathfrak{C} \in [0.1, 1]$, which is a practically reasonable range. Colors represent meshes going from lower aspect ratio (yellow) to higher aspect ratio (blue). Color-shaded areas depict variation of $\mathfrak{C}$ with $\hat{k}$ and θ, while color-lines plot the average values of $\mathfrak{C}$. Plot-rows indicate length-scale strategies and plot-columns vary the Peclet number Pe. For details on construction of the sub-figures, see Appendix C.

Table 5: Minimum, average and maximum values of $\mathfrak{C}_{\text{max}}$ with different length-scale strategies at varying Pe on **three-dimensional domains** (see Sub-section 3.4.3 and Figure 9). Each set of minimum-mean-maximum values encapsulates variation with respect to p, $\hat{k}$, θ and ϕ.

Pe:	1			10^6		
	min	mean	max	min	mean	max
GD1-GG1	0.32	0.77	2.6	0.41	0.65	1.3
GS1	0.012	0.14	1.1	0.16	5.6	220
GS2	0.007	0.21	0.85	0.1	5.5	109
GG2	0.011	0.057	0.35	0.15	3.3	130

3.4.3. Extension to $\mathcal{D} = 3$

As stated earlier, the proposed length-scale strategy GD1-GG1 extends seamlessly to higher dimensions. This is shown by considering three $5 \times 5 \times 5$ meshes with $\mathcal{D} = 3$: the first is a regular cube, the second is a parallelepiped, and the third a cuboid with extremely thin width in the x_3 (see Figure 2). In addition to azimuthal variation of the advection direction $\theta \in [0, \pi]$, we also vary its elevation $\phi \in [0, \pi]$. To have reasonable turnaround times, Pe $\in \{1, 10^6\}$ and $p \in [1, 6]$ are used. Figure 9 shows the results of the analysis. For both Pe $= 1$ and Pe $= 10^6$, GD1-GG1 outperforms the other strategies, successfully keeping $\mathfrak{C}$ in a reasonable range for attaining Δt_{max}. As expected, the benefit compounds for the skewed and high-aspect ratio meshes.

Both the 2D and 3D VNA conducted in the preceeding sub-sections confirm the generality of the proposed length-scale computation strategy GD1-GG1.

4. Studies on Navier-Stokes system

In this section, we extend the length-scale estimation strategy GD1-GG1 to the Navier-Stokes system of equations. As discussed before, a robust timestep estimation strategy should predict a stable timestep close to and within the stability limit, with minimum variation in the CFL number $\mathfrak{C}$ across a wide range of polynomial-orders, cell-quality and flow physics (e.g. the Reynolds number Re, the Mach number M). The typical range of CFL numbers used by engineers for practical industrial simulations is $\mathfrak{C} \in [0.1, 1]$; a good timestep calculator should provide stable, near-limit estimates without requiring the CFL number to stray too far outside these limits. We study two cases: the first case uses explicit timestepping on a flow in equilibrium. It covers skewed meshes, low, medium and high Re, subsonic and supersonic M, and high p to show the effectiveness of the proposed strategy across these wide variety of configurations. In Appendix D, we additionally show that no spurious oscillations are introduced when running near the stability limit. The second case a is steady turbulent flow past a multi-element airfoil, through which we demonstrate the proposed strategy for a representative external-aerodynamics case on a distorted curved mesh. The second case also highlights the application of the proposed strategy to local-timestepping for p-multigrid based
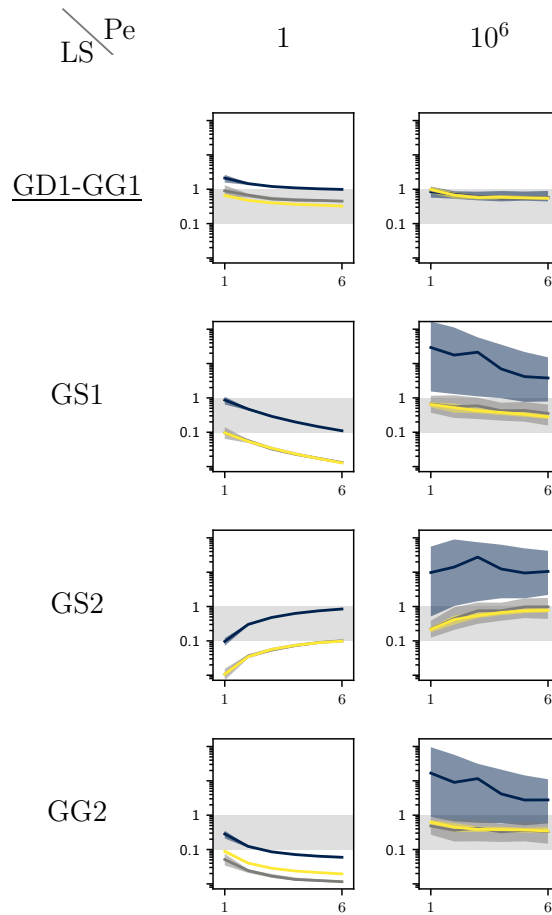
Fig. 9: Results of VNA on **three-dimensional domains** (see Sub-section 3.4.3 and Table 5). Maximum CFL number $\mathfrak{C}_{max}$ in log-scale (ordinate of each sub-plot) plotted against increasing polynomial-orders $p \in [1, 6]$ (abscissa of each sub-plot). All sub-plots share the same limits on the axes. The grey-shaded area marks the region of $\mathfrak{C} \in [0.1, 1]$, which is a practically reasonable range. Colors represent meshes: square (yellow), parallelepiped (ash), and high aspect ratio (blue). Color-shaded areas depict variation pf $\mathfrak{C}$ with $\hat{k}$ and θ, while color-lines plot the average values of $\mathfrak{C}$. Plot-rows indicate length-scale strategies and plot-columns indicate varying Pe. For details on construction of the sub-figures, see Appendix C.

335   convergence acceleration.

4.1. Governing equations

337   The representative system is the compressible unsteady RANS equations in conservative form for a Newtonian

338   working fluid. The temperature dependence of fluid viscosity is modeled using Sutherland's law [28]. Eddy viscosity

339   is obtained using the modified Spalart-Allmaras (SA) turbulence model [29] to ensure numerical stability in the

340   presence of negative values of the turbulence variable ϑ, especially with coarse spatial discretization of the boundary

341   layer edge. The governing equations are cast into the following compact form:

$$\partial_t \boldsymbol{U} + \sum_{j=1}^{\mathcal{D}} \partial_j (\boldsymbol{F}_{\text{ivc}} + \boldsymbol{F}_{\text{vsc}}) = \boldsymbol{S} \tag{27}$$

343   where $\boldsymbol{U} \in \mathbb{R}^{1 \times \mathcal{N}}$ is the solution-vector, $\boldsymbol{F}_{\text{ivc}} \in \mathbb{R}^{\mathcal{D} \times \mathcal{N}}$ and $\boldsymbol{F}_{\text{vsc}} \in \mathbb{R}^{\mathcal{D} \times \mathcal{N}}$ are the inviscid- and viscous-flux-vectors

344   respectively, and $\boldsymbol{S} \in \mathbb{R}^{1 \times \mathcal{N}}$ is the source-term-vector. $\mathcal{N}$ is the number of solution-variables and $\mathcal{D}$ is the spatial

345   dimension. More precisely:

$$\boldsymbol{U} = \begin{bmatrix} \rho & \rho v_1 & \rho v_2 & \rho v_3 & \rho E & \rho \vartheta \end{bmatrix}^T, \tag{28}$$

$$\boldsymbol{F}_{\text{ivc}} = \begin{bmatrix} \rho v_1 & \rho v_2 & \rho v_3 \\ p + \rho v_1 v_1 & \rho v_1 v_2 & \rho v_1 v_3 \\ \rho v_2 v_1 & p + \rho v_2 v_2 & \rho v_2 v_3 \\ \rho v_3 v_1 & \rho v_3 v_2 & p + \rho v_3 v_3 \\ \rho v_1 H & \rho v_2 H & \rho v_3 H \\ \rho v_1 \vartheta & \rho v_2 \vartheta & \rho v_3 \vartheta \end{bmatrix}, \tag{29}$$

$$\boldsymbol{F}_{\text{vsc}} = \begin{bmatrix} 0 & 0 & 0 \\ -\tau_{11} & -\tau_{12} & -\tau_{13} \\ -\tau_{21} & -\tau_{22} & -\tau_{23} \\ -\tau_{31} & -\tau_{32} & -\tau_{33} \\ -v_1\tau_{11} - v_2\tau_{21} - v_3\tau_{31} - \omega_1 & -v_1\tau_{12} - v_2\tau_{22} - v_3\tau_{32} - \omega_2 & -v_1\tau_{13} - v_2\tau_{23} - v_3\tau_{33} - \omega_3 \\ -\frac{\eta}{\sigma}\partial_1\vartheta & -\frac{\eta}{\sigma}\partial_2\vartheta & -\frac{\eta}{\sigma}\partial_3\vartheta \end{bmatrix}, \tag{30}$$

$$\boldsymbol{S} = \begin{bmatrix} 0 & 0 & 0 & 0 & 0 & \mathcal{G} - \mathcal{Y} + \mathcal{K} + \mathcal{T} \end{bmatrix}^T. \tag{}$$

353   The symbols used in the equations above are: ρ is the density, v_1, v_2 and v_3 are the velocity-components in the three

354   coordinate-directions, E is the total energy per unit mass, i.e. $E = e + \frac{1}{2}(v_1 v_1 + v_2 v_2 + v_3 v_3)$ where e is the internal

355   energy. For a calorically perfect gas, $e = \frac{RT}{\gamma - 1}$ where R is the gas constant and T is the temperature determined as

356    $T = \gamma M^2 p / \rho$ where M is the Mach number. The total enthalpy H is defined as $H = E + \frac{p}{\rho}$ where p is the pressure,

357   related to energy through the ideal gas law:

$$p = \rho(\gamma - 1)\left(E - \frac{1}{2}(v_1 v_1 + v_2 v_2 + v_3 v_3)\right) \tag{31}$$

359 where γ is the specific heat ratio. τ_{ij} are the components of the viscous stress tensor $\underline{\underline{\tau}}$. For compressible Newtonian

360 fluids:

$$\tau_{ij} = 2(\mu + \mu_t)S_{ij} \quad , \quad S_{ij} = \frac{1}{2}\left(\partial_i v_j + \partial_j v_i\right) - \frac{1}{3}\delta_{ij}\left(\partial_1 v_1 + \partial_2 v_2 + \partial_3 v_3\right) \tag{32}$$

362 where μ_t is the eddy viscosity and μ is the dynamic viscosity which is determined as a function of temperature through

363 Sutherland's law. The symbol $\omega_j = (\lambda + \lambda_t)\partial_j T$ is the j-th component of the heat flux vector where $\lambda = \frac{\gamma R}{\gamma-1}\frac{\mu}{\text{Pr}}$ is the

364 molecular conductivity and $\lambda_t = \frac{\gamma R}{\gamma-1}\frac{\mu_t}{\text{Pr}_t}$ is the eddy conductivity. Unless specified otherwise, laminar Prandtl number

365 $\text{Pr} = 0.72$ and turbulent Prandtl number $\text{Pr}_t = 0.9$ are used. The details of computing eddy-viscosity μ_t as a function

366 of $\rho\vartheta$, as well as those of computing the production ($\mathcal{G}$), destruction ($\mathcal{Y}$) and diffusion-correction ($\mathcal{K}$) source-terms

367 and the turbulent diffusion-coefficient η are taken as-is from [29]. The trip term ($\mathcal{T}$) is set to zero, as we are modeling

368 fully turbulent flows. Distance to the airfoil-walls is approximated as the distance to the nearest discrete-point on the

369 airfoil-walls.

370 *4.2. p-multigrid*

371 The semi-discrete form of (5) is accelerated to steady state using a p-multigrid full approximation scheme (FAS)

372 proposed by Fidkowski et al. [30]. Standard Runge-Kutta-54 scheme is used as a smoother. Restriction of the solution

373 and prolongation of the correction on the p-levels is performed using an $\mathbb{L}^2$ projection. To prevent limit-cycles, the

374 correction from polynomial-order $i-1$ to polynomial-order i is damped / under-relaxed by multiplying by a factor

375 $\alpha_{i-1}^i \in (0,1]$. In all simulations, $\alpha_{i-1}^i = 0.9$ for $i < p$ and $\alpha_{i-1}^i = 0.1$ for $i = p$. A standard sweep-pattern of

376 1-2-3-4-...-p is used for the multigrid sweeps after restriction, and a similar reverse pattern of p-$p-1$...-4-3-2-1 is

377 used for smoothing the corrected solution after prolongation. Since we are interested in the steady-state solution,

378 time-accuracy is not important. We therefore can take as large a timestep as permissible by stability limits, which can

379 vary from cell-to-cell.

380 *4.3. Time-step calculation*

381 Recall the definition of the convective length-scale $\mathfrak{h}_p^{\text{con}}$ from Sub-section 3.2. At a given solution-point j of cell

382 i, let $\boldsymbol{l}_{ij}^{\text{con}}$ be the vector that defines it, such that $\left[\mathfrak{h}_p^{\text{con}}\right]_{ij} = \left\|\boldsymbol{l}_{ij}^{\text{con}}\right\|$ (see Figure 10). Also, let $\hat{\boldsymbol{l}}_{ij}^{\text{con}}$ be the corresponding

383 unit-vector. The propagation of compressibility effects through the speed of sound c, defined as

$$c = \sqrt{\frac{\gamma p}{\rho}}, \tag{33}$$

385 is not necessarily aligned with the velocity-vector $\boldsymbol{v}$. Since c propagates in all directions [31, 32], we consider the

386 shortest distance between the solution-point and the sub-cell-diagonal (represented by the vector $\boldsymbol{l}^{\text{sos}}$ in Figure 10) to

387 define the speed of sound length-scale. Thus, considering all sub-cells (recall Figure 4) that the j-th solution-point is

388 part of, $\left[\mathfrak{h}_p^{\text{sos}}\right]_{ij} = \min_k \left\|\boldsymbol{l}^{\text{sos}}_{ijk}\right\|$ where k is an index over the sub-cells. The corresponding vector and unit-vector are

389 $\boldsymbol{l}_{ij}^{\text{sos}}$ and $\hat{\boldsymbol{l}}_{ij}^{\text{sos}}$.
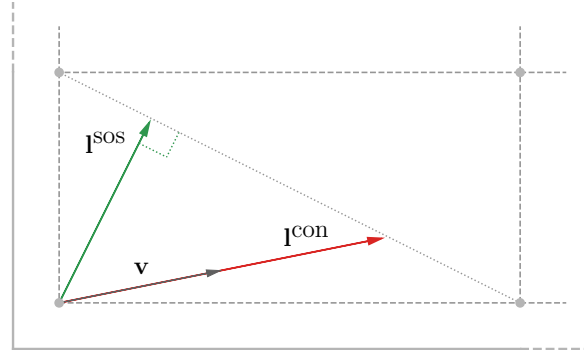
Fig. 10: Schematic depicting the difference between the convective length-scale vector l^{con} and the speed-of-sound length-scale vector l^{sos} for a given solution-point in a given sub-cell. l^{con} is the convective length-scale vector in the direction of the flow-velocity, as defined in Sub-section 3.2. l^{sos} is the shortest possible convective length-scale vector for the given solution-point in the given sub-cell.

Having defined these, for a given cell C_i with the j-th index iterating over all its solution-points, the local time-step is computed as

$$\Delta t_{i,\text{dif}} = \min_{j} \frac{\left[\mathfrak{h}_p^{\text{dif}}\right]_i^2}{\nu_{ij} + \dfrac{\mu_{t_{ij}}}{\rho_{ij}}}, \tag{34a}$$

$$\Delta t_{i,\text{sos}} = \min_{j} \frac{\left[\mathfrak{h}_p^{\text{sos}}\right]_{ij}}{c + \left|\boldsymbol{v}_{ij} \cdot \hat{\boldsymbol{l}}_{ij}^{\text{sos}}\right|}, \tag{34b}$$

$$\Delta t_{i,\text{con}} = \min_{j} \frac{\left[\mathfrak{h}_p^{\text{con}}\right]_{ij}}{c + \left\|\boldsymbol{v}_{ij}\right\|}, \tag{34c}$$

$$\Delta t_i = \mathfrak{C} \min\left(\Delta t_{i,\text{dif}} \quad, \quad \Delta t_{i,\text{sos}} \quad, \quad \Delta t_{i,\text{con}}\right). \tag{34d}$$

This is the GD1-GG1 strategy adapted for the Navier-Stokes equations. Some important observations about the timestep estimator are presented below:

- Equation (34a): Typically $\mathfrak{h}_p^{\text{dif}} < \mathfrak{h}_p^{\text{con}}$, and thus $\left(\mathfrak{h}_p^{\text{dif}}\right)^2 \ll \mathfrak{h}_p^{\text{con}}$. For low Re flows therefore, the timestep computed from the diffusive part is the limiting timestep. This can also be the case for high Re flows where the cell-sizes are very small, and/or where the eddy-viscosity attains high values. Note the presence of μ_t in (34a).

- Equation (34b): For high Re flows with Mach-number M < 1, we have $c > \|\boldsymbol{v}\|$. Since $\mathfrak{h}_p^{\text{sos}} < \mathfrak{h}_p^{\text{con}}$, it is the speed of sound that determines the limiting timestep. In this case, the maximum eigenvalue of the inviscid Jacobian is the sum of the speed of sound and the velocity-component in the direction of propagation [32]. As discussed before, the stability-limiting direction of propagation of the speed-of-sound is the direction along
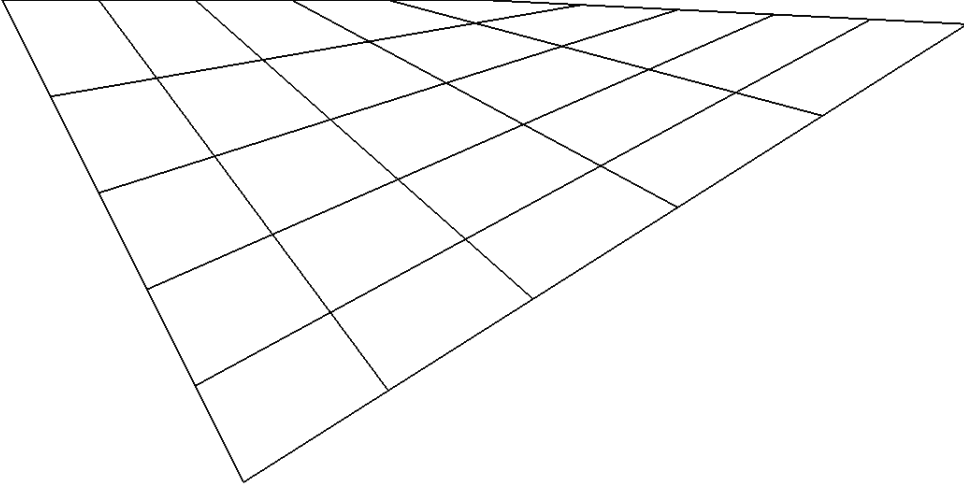
Fig. 11: An example of a mesh with highly obtuse cells used in the "Case C" tests of Sub-section 4.4.

which the distance from the j-th solution-point to any neighboring sub-cell diagonal is the shortest. Recall that this direction is given by $\hat{\boldsymbol{l}}_{ij}^{\text{sos}}$. Therefore, the velocity component in this direction is given by $\boldsymbol{v}_{ij} \cdot \hat{\boldsymbol{l}}_{ij}^{\text{sos}}$. We take its absolute-value to account for the case where $\boldsymbol{v}_{ij} \cdot \hat{\boldsymbol{l}}_{ij}^{\text{sos}}$ points opposite to $\hat{\boldsymbol{l}}_{ij}^{\text{sos}}$.

- Equation (34c): For high Re flows with M > 1, we have $c < \|\boldsymbol{v}\|$ and there is a possibility that the flow-velocity determines the limiting timestep. We take the entire magnitude of c in the direction of $\boldsymbol{v}$ due to the omnidirectional nature of c.

For time-accurate explicit timestepping, the global timestep is computed as the minimum of all cell-local timesteps. Watkins et al. recommend using a harmonic mean of the convective and diffusive estimates [15]. However, we observed that this led to overtly conservative estimates. The performance of the proposed length-scale strategy is compared with the other three strategies described in Sub-section 3.4, namely GS1, GS2 and GG2. Note that, other than the strategy of computing $\mathfrak{h}_p^{\text{con}}$ and $\mathfrak{h}_p^{\text{dif}}$, *no other numerics settings are changed for any of the runs*. All runs use exactly the same numerical parameters.

4.4. Explicit timestepping: the "do nothing" scenario

The first test is that of a simple domain initialized with constant equilibrium values of all flow-variables and Riemann-invariant boundaries [33]. This case is run for $p \in [1, 10]$, Re $\in \{1, 10^4, 10^8\}$, M $\in \{0.1, 0.5, 2\}$, and angle of incidence $\theta \in \{0, \pi/4, \pi/2\}$. The effect of mesh-quality is assessed by studying the behavior on three series of meshes, each containing 5×5 cells:

- Skewed meshes (Case A): similar to Sub-section 3.4.1 (see M_*^{a} series in Figure 2), the meshes are shear-skewed in the negative and positive directions by $60°$.

- High-aspect-ratio meshes (Case B): similar to Sub-section 3.4.2 (see M_*^{b} series in Figure 2), the meshes are gradually increased in aspect-ratio as 1, 10, 100 and 1000.

Table 6: Minimum, average and maximum values of $\mathfrak{C}_{max}$ for the Navier-Stokes equations with different length-scale strategies and mesh-skewness types (see Sub-section 4.4 and Figure 12). Each set of minimum-mean-maximum values encapsulates variation with respect to p, Re, M and θ.

Skewness type:	A			B			C		
	min	mean	max	min	mean	max	min	mean	max
GD1-GG1	0.41	0.85	1.9	0.36	0.77	1.7	0.78	2.1	6.4
GS1	0.044	1.1	4.8	0.05	1.1	4.2	0.02	1.4	7.8
GS2	0.071	2.1	6.4	0.074	2.4	5.5	0.14	2.6	5.5
GG2	0.025	0.53	2.7	0.002	0.26	1.1	0.045	0.62	2.3

- Meshes with obtuse angles (Case C): In some instances, mesh-cells contain corners with highly obtuse angles while the rest of the cell itself is of relatively good shape. This series contains meshes with gradually more obtuse corners. An example of such a mesh is given in Figure 11.

Thus, for each mesh, at each p, we analyze 27 flow-scenarios across Re, M and θ. For each scenario we record $\mathfrak{C}_{max}$, the maximum CFL that maintains a stable equilibrium in the domain.

Figure 12 provides an overview of the results. Looking at the first column (Case A), GD1-GG1 generalizes well on the range of shear-skewed meshes for all polynomial orders. It is resilient to aforementioned changes in flow-physics (Re, M and θ), as indicated by the narrow colored-bands. In comparison, the other strategies show significant mesh and p dependence. The wider bands for the other strategies also reveal their sensitivity to flow-physics. The improved behavior of GD1-GG1 also extends to meshes with high aspect-ratios (Case B). For meshes with highly obtuse cells (Case C), the generalization is less strong for GD1-GG1 with $\mathfrak{C}_{max}$ reaching values upto 5 for the worst quality meshes. However, the estimates are on the conservative side, and the variation reduces as the order is increased. In any case, the variation is much lower in comparison to the other strategies - GS1 for instance shows variation between 0.01 and 8. These results show the effectiveness of the proposed strategy for predicting the optimal timestep for flows governed by the NS-equations advanced using explicit timestepping. Additionally, in Appendix D we show that no spurious oscillations are introduced when running near the stability limit.

4.5. p-multigrid with LTS on distorted curved meshes: Turbulent flow past a multi-element airfoil

In this test, we study the effect of length-scale calculation strategy on the convergence behavior of p-multigrid with LTS. Since every cell is advanced in time with an independent timestep, it is paramount that the predicted cell-local length-scale be close to its ideal value. The case is a turbulent flow past a multi-element airfoil [34] at Re $= 9 \times 10^6$, M $= 0.2$ and angle-of-attack $16°$. The walls of the airfoil are modeled as no-slip adiabatic walls, while the far-field is modeled as a characteristic boundary. The flow is initialized with freestream values, and accelerated to convergence.

The mesh used is the 4th-order curved quadrilateral mesh provided in the workshop, consisting of roughly 4000 cells. It is well suited for stress-testing the LTS computation, as it contains skewness of all types we have analyzed
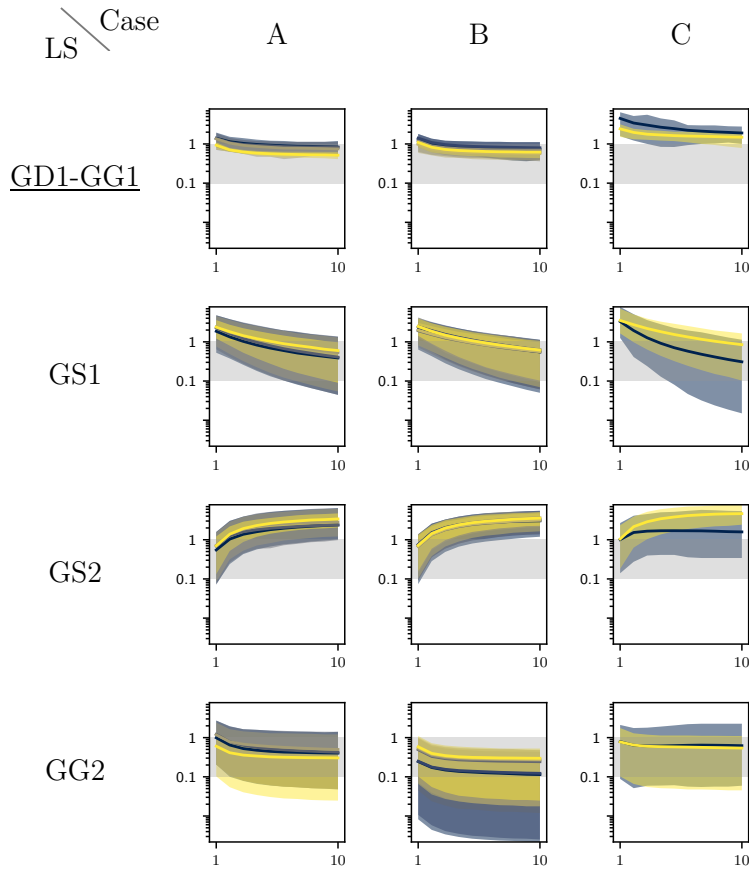
Fig. 12: Results of equilibrium tests with the Navier-Stokes equations on cases A, B, and C from Sub-section 4.4 (quantitative summary in Table 6). Maximum CFL number $\mathfrak{C}_{max}$ in log-scale (ordinate of each sub-plot) plotted against increasing polynomial-orders $p \in [1, 10]$ (abscissa of each sub-plot). All sub-plots share the same limits on the axes. The grey-shaded area marks the region of $\mathfrak{C} \in [0.1, 1]$, which is a practically reasonable range. Plot-rows indicate length-scale strategies and plot-columns indicate the different types of mesh-skewness. Colors represent mesh-quality: good (yellow) to bad (blue). Color-shaded areas depict variation of $\mathfrak{C}$ with Re, M and θ, while color-lines plot the average values of $\mathfrak{C}$.
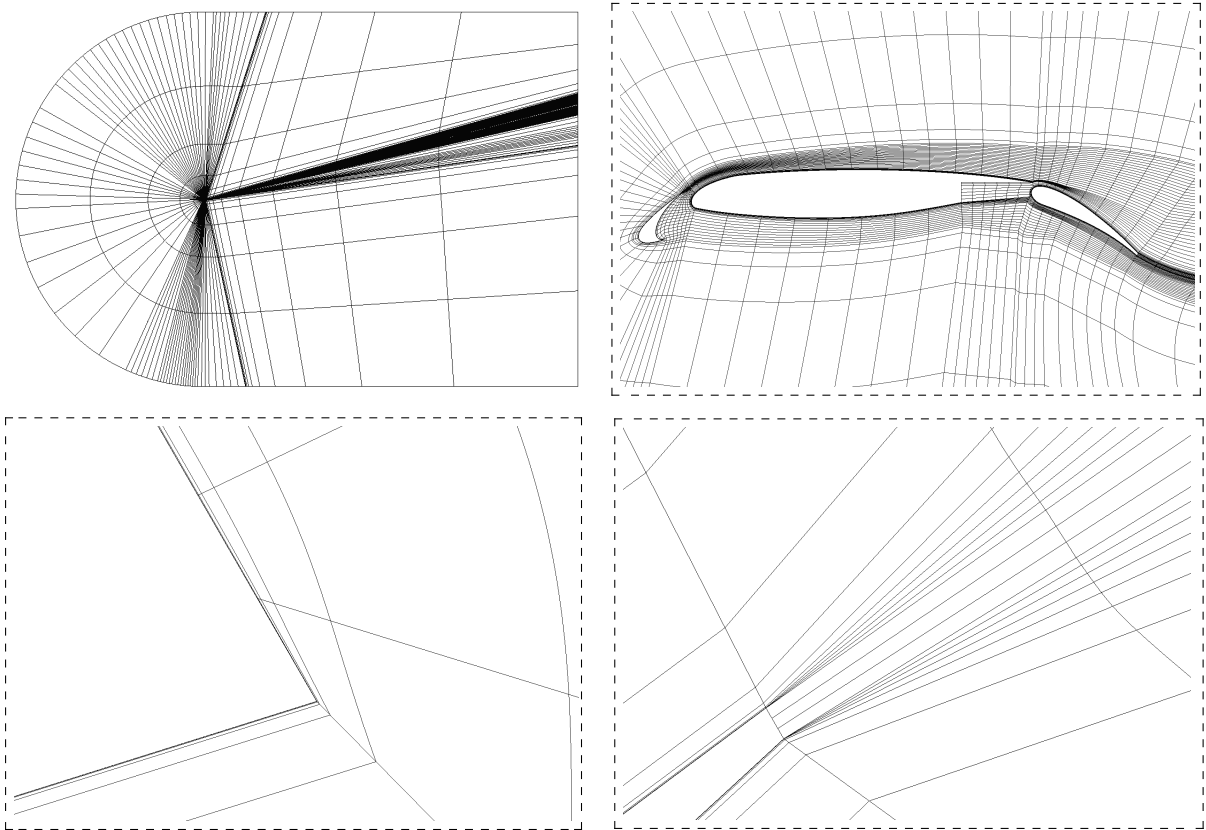
Fig. 13: 4th-order curved quadrilateral mesh for the multi-element airfoil provided in the 2015 edition of the high-order workshop [34], used in the simulations of Sub-section 4.5. Note the presence of cells with high aspect-ratio, high obtuse-angles and shear-skewness. In some cases, the jump in size of adjacent cells reaches a factor of 50.
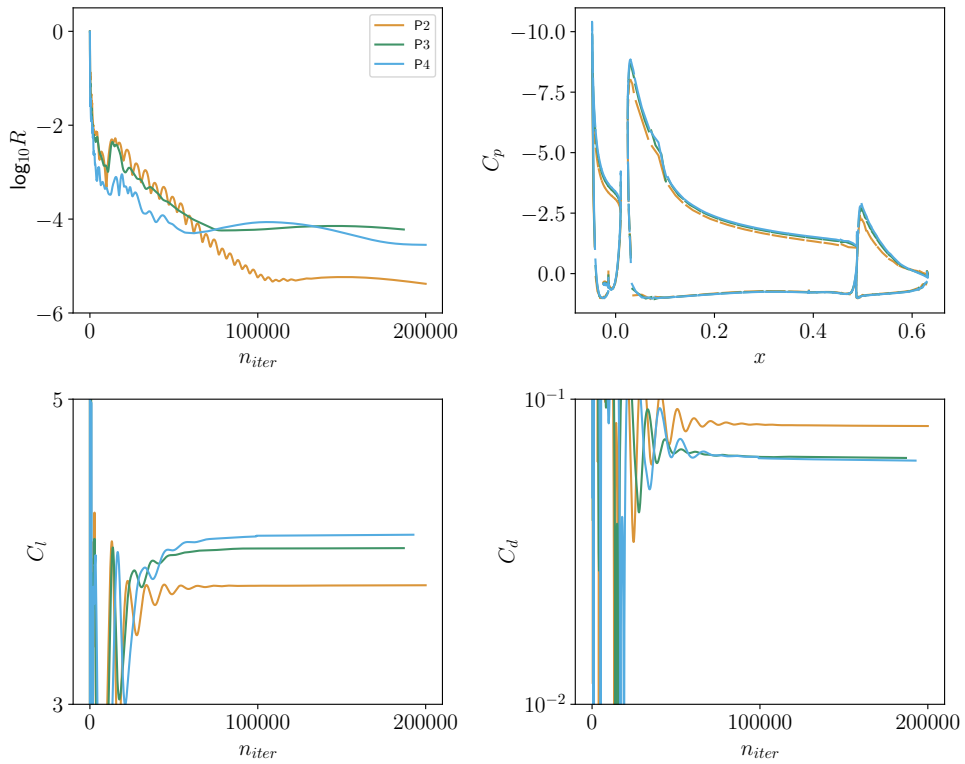
Fig. 14: Pressure-coefficient distribution and convergence history of relative residuals, lift- and drag-coefficients for the multi-element airfoil.

in this paper - distorted cells, high aspect-ratio cells, and cells with large obtuse angles (see Figure 13). Cell-sizes range from 10^{-8} units to 10^2 units. We run the multi-element airfoil case for $p \in [2, 4]$. Local timesteps are computed using the length-scale strategy GD1-GG1. The $\mathfrak{C}$ used is 0.4 for $p \in [2, 4]$. Convergence of residuals, lift- and drag-coefficients, along with pressure-coefficient distribution, is shown in Figure 14. We see that the case successfully executes without needing much variation of the $\mathfrak{C}$ number, despite the presence of highly distorted cells in the mesh. Using higher values of $\mathfrak{C}$ leads to divergence, indicating that the selected $\mathfrak{C}$ is close to the stability limit. Runs with the other three length-scale strategies lead to unstable simulations, for any choice of $\mathfrak{C} \in [0.1, 1]$. Furthermore, absence of LTS heavily slows down the computation, with the residuals needing $\sim 10^7$ V-cycles to drop two orders of magnitude. In comparison, for the aforementioned p-multigrid with LTS using GD1-GG1, the residuals take ~ 80000 V-cycles to drop four orders of magnitude. This highlights the value of local-timestepping for faster convergence, and makes the correct prediction of maximum local-timesteps all the more important. The GD1-GG1 strategy achieves this where other strategies fail.

We now analyze what choice of $\mathfrak{C}$ is required for stable simulations when using the other strategies. This is done as follows: we know from previous analyses that GD1-GG1 yields close to the maximum possible timestep independent of the cell-shape and polynomial-order. If convection dominates in a given cell C_i and $c_i \gg |\mathbf{v}_i|$, then from (34b) we get

$$\Delta t_i = \mathfrak{C}_{\text{GD1-GG1}} \frac{\left[\mathfrak{h}_p^{\text{sos}}\right]_{i,\text{GD1-GG1}}}{c_i}. \tag{35}$$

To get the same Δt_i using a different length-scale strategy denoted by the subscript S, the necessary $\mathfrak{C}$ value in that cell can be determined by equating the two timesteps as

$$\mathfrak{C}_{S,i} \frac{\left[\mathfrak{h}_p^{\text{sos}}\right]_{i,S}}{c_i} = \mathfrak{C}_{\text{GD1-GG1}} \frac{\left[\mathfrak{h}_p^{\text{sos}}\right]_{i,\text{GD1-GG1}}}{c_i},$$
$$\mathfrak{C}_{S,i} = \mathfrak{C}_{\text{GD1-GG1}} \frac{\left[\mathfrak{h}_p^{\text{sos}}\right]_{i,\text{GD1-GG1}}}{\left[\mathfrak{h}_p^{\text{sos}}\right]_{i,S}}. \tag{36}$$

Similarly, for diffusion-dominated cells, the necessary $\mathfrak{C}$ to yield the same timestep as that of GD1-GG1 in each of those cells would be

$$\mathfrak{C}_{S,i} = \mathfrak{C}_{\text{GD1-GG1}} \left(\frac{\left[\mathfrak{h}_p^{\text{dif}}\right]_{i,\text{GD1-GG1}}}{\left[\mathfrak{h}_p^{\text{dif}}\right]_{i,S}}\right)^2. \tag{37}$$

Taking $\mathfrak{C}_{\text{GD1-GG1}} = 0.4$ from earlier simulations of the multi-element airfoil, using (36) and (37) we compute in each cell C_i the necessary $\mathfrak{C}_{S,i}$ for the other three length-scale strategies - first assuming convection-dominated flow, and then assuming diffusion-dominated flow. The smaller the value of $\mathfrak{C}_{S,i}$ in cell C_i, the greater is the overprediction of the length-scale in that cell (and vice versa). We then create bins of $\mathfrak{C}_{S,i}$, each bin spanning an order of magnitude (e.g. 0.1 to 0.01, 0.01 to 0.001, etc.), and count how many cells each bin contains. The results are plotted as histograms in Figure 15. Some important observations are discussed below:

- Assuming convection-dominated flows in all cells, the GS1 strategy predicts the cell-local length-scale quite well in most of the cells. This is evident from most of the cells lying in the 1 to 0.1 bin. However, for $p > 2$, a
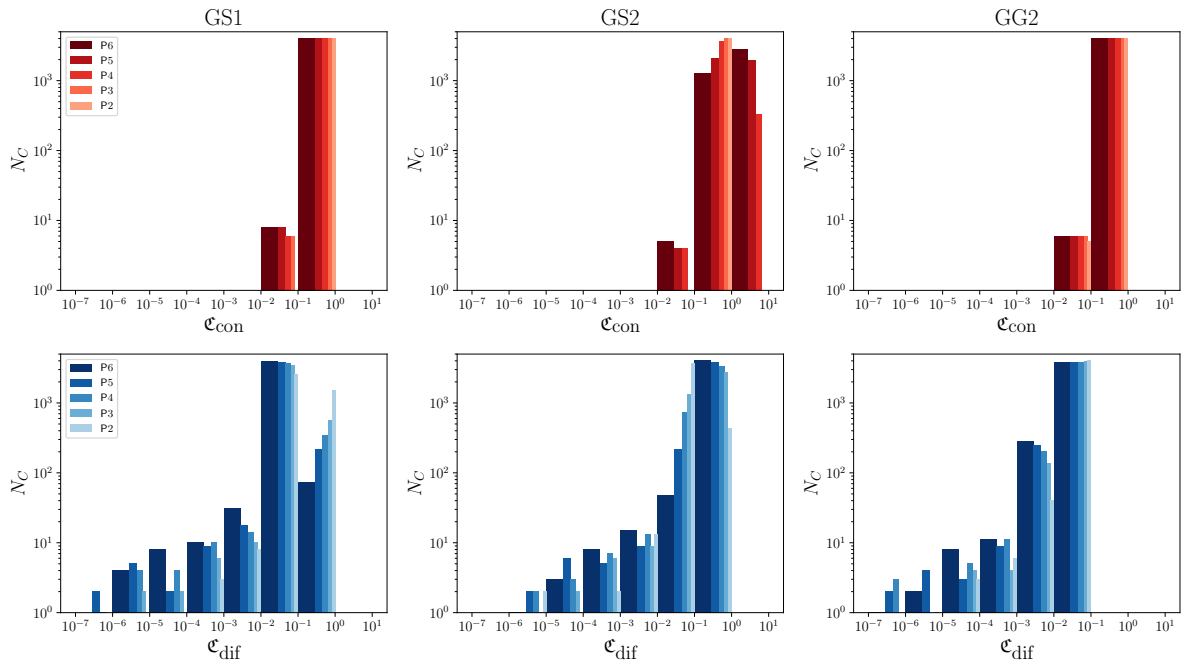
Fig. 15: Histograms depicting the cell-wise $\mathfrak{C}$ required to match the LTS values of the GD1-GG1 strategy in each cell. Abcissa contains $\mathfrak{C}$-bins, with each bin spanning an order of magnitude. Ordinate indicates, for a given bin, the number of cells which require the $\mathfrak{C}$ to be in that range so that a stable timestep can be obtained. First row of plots assumes convection-dominated flow in all cells, showing that some cells demand $0.01 < \mathfrak{C} < 0.1$. Second row of plots assumes diffusion-dominated flow in all cells, showing potentially drastic values of $\mathfrak{C}$, sometimes in the range of 10^{-6}.

handful of cells lie in the 0.1 to 0.01 bin. This means that, to ensure stability, the global $\mathfrak{C}$ might need to drop below 0.1. This might degrade the convergence in the other majority of cells.

- The same reasoning extends to the GG2 and GS2 strategies. In addition, GS2 makes a conservative estimate in many cells for $p > 3$ (as shown by the large cell-count in the 1-to-10 bin). Thus, using $\mathfrak{C} < 0.1$, the convergence in those cells will be even more sub-optimal.

- The situation is much more dire if we assume diffusion-dominated flows, irrespective of which of the three strategies is chosen. While a large majority of cells fall in the bins between 1 and 0.01, the diffusive length-scale is severely overpredicted in handful of cells. Thus, if diffusion comes to dominate in those cells, the global $\mathfrak{C}$ value might need to be dropped to unreasonably small values.

We thus observe a large uncertainty in the appropriate $\mathfrak{C}$ value when using legacy length-scale estimation strategies. This is aggravated by the fact that the growth of eddy-viscosity happens gradually over the course of convergence. This means, that cells which were convection-dominated early on in the simulation might come to be diffusion-dominated much later. Thus, even if the $\mathfrak{C}$ value was somehow sufficient up to that point, it might not suffice any longer and cause divergence. The potential wastage of time and computational resources is significant. Even if a stable $\mathfrak{C}$ is found through trial-and-error for legacy strategies, the rate of convergence would be extremely poor, making p-multigrid with LTS infeasible. The proposed GD1-GG1 strategy mitigates this risk.

5. Conclusion

We propose a robust cell-local length-scale estimation strategy GD1-GG1 for the flux-reconstruction framework. The strategy directly uses the geometric and polynomial discretization within each cell to separately estimate the convective and diffusive length-scales. We theoretically demonstrate its generalization to highly skewed meshes (shear-skewness and high aspect-ratios) through two- and three-dimensional von-Neumann analysis on the advection-diffusion equation. A large parameter-space is explored by varying the wavelength of the incoming signal, the direction of propagation, and the Peclet number. The proposed method restricts the variation of the CFL-number to a practically reasonable range of 0.1 to 1 for polynomial-orders ranging between 1 and 10, in contrast to legacy strategies which show CFL-variation across orders of magnitude.

The GD1-GG1 strategy is extended to the density-based RANS system of equations, taking into account both the directional behavior of the flow-velocity and the omnidirectional behavior of the speed of sound. Its robustness is assessed on meshes with a variety of cell-distortions (shear-skewness, high aspect-ratios, high obtuse-angles) and large variations in the flow-physics through the Reynolds and Mach numbers. Finally, we demonstrate its benefit for cases of practical interest through steady-state RANS-modeled turbulent flow over the multi-element airfoil. The solution is driven to steady-state using a combination of local-timestepping and p-multigrid. A high-order curved mesh containing highly distorted cells is used, with polynomial-orders ranging from 2 to 5. The maximum stable CFL-number remains fixed around 0.3 to 0.4. Through assessing the length-scale distribution of legacy strategies on

the same case, we highlight their lack of generality and the subsequent risks of wastage of time and computational resources. In conclusion, the proposed length-scale estimation strategy promises to be a useful ingredient in industry-grade high-order flux-reconstruction solvers by freeing engineers from having to determine the optimal CFL number on a case-to-case basis. It also avoids potentially expensive wastage of time and resources.

In subsequent works, this study needs to be extended to other types of elements, such as triangles, tetrahedra, prisms, etc. that are widely used in industrial meshes.

Conflict of interest

The work presented in this paper does not have any conflict of interest with other organizations.

Appendix A. Fully discrete scheme

From Section 2 we see that the semi-discrete form (5) is a function of U^δ, Q^δ and S^δ. Since the latter two can be computed from U^δ, we can write (5) as

$$\partial_t U = \text{RHS}\left(U^\delta\right). \tag{A.1}$$

With a time-step Δt, the RK33 scheme advances the solution $U^{\delta,n}$ to $U^{\delta,n+1}$ as

---
Algorithm 1 RK33

$k_1 \leftarrow \Delta t \text{RHS}\left(U^{\delta,n}\right)$

$k_2 \leftarrow \Delta t \text{RHS}\left(U^{\delta,n} + \frac{k_1}{2}\right)$

$k_3 \leftarrow \Delta t \text{RHS}\left(U^{\delta,n} - k_1 + 2k_2\right)$

$U^{\delta,n+1} \leftarrow U^{\delta,n} + \frac{1}{6}\left(k_1 + 4k_2 + k_3\right)$

Appendix B. Assembly of VNA matrices

Here, we present the details of assembling the element-wise matrices that are used in the VNA of Sub-section 3.1. For convenience, we introduce the following standard notation for averages and jumps:

$$\{\cdot\}_{a,b} = \frac{(\cdot)_a + (\cdot)_b}{2} \tag{B.1}$$

$$[\![\cdot]\!]_{a,b} = (\cdot)_a - (\cdot)_b$$

Applying the flux-reconstruction discretization, we get the following semi-discrete form of the advection-diffusion equation (14) in C_O (for readability, subscript skipped until otherwise stated)

$$\partial_t u = -\nabla^\delta\left(F^\delta + G^\delta\right). \tag{B.2}$$

Under the influence of the element Jacobian $\mathbf{J}$ (known), we have

$$
\begin{aligned}
\nabla^\delta \left(\boldsymbol{F}^\delta + \boldsymbol{G}^\delta \right) = & \hat{\nabla}^\delta \mathbf{J}^{-1} \left(\boldsymbol{F}^{\delta\mathrm{D}} + \boldsymbol{G}^{\delta\mathrm{D}} \right) \\
& + \mathbf{J}^{-1} \left(d\hat{\boldsymbol{F}}^{\delta\mathrm{C}} + d\hat{\boldsymbol{G}}^{\delta\mathrm{C}} \right).
\end{aligned}
\tag{B.3}
$$

Here $\hat{\nabla}^\delta$ is the gradient of the Lagrange interpolation polynomials in reference space (known). $\boldsymbol{F}^{\delta\mathrm{D}}$ is the discontinuous inviscid flux evaluated using the discontinuous solution $u^{\delta\mathrm{D}}$ (known) and (14). $\boldsymbol{G}^{\delta\mathrm{D}}$ is the discontinuous viscous flux computed using gradients of the *corrected* solution $\nabla^\delta u^{\delta\mathrm{C}}$. We will return to the other terms of (B.3) shortly. The gradient of the corrected solution is calculated as

$$
\nabla^\delta u^{\delta\mathrm{C}} = \hat{\nabla}^\delta \mathbf{J}^{-1} u^{\delta\mathrm{D}} + \mathbf{J}^{-1} d\hat{u}^{\delta\mathrm{C}},
\tag{B.4}
$$

where $d\hat{u}^{\delta\mathrm{C}}$ is the gradient of the solution-correction in reference space, i.e.

$$
d\hat{u}^{\delta\mathrm{C}} =
\begin{bmatrix}
\hat{h}_l \left(u_l{}^{\delta\mathrm{I}} - u_l{}^{\delta\mathrm{F}} \right) + \hat{h}_r \left(u_r{}^{\delta\mathrm{I}} - u_r{}^{\delta\mathrm{F}} \right) \\
\hat{h}_b \left(u_b{}^{\delta\mathrm{I}} - u_b{}^{\delta\mathrm{F}} \right) + \hat{h}_t \left(u_t{}^{\delta\mathrm{I}} - u_t{}^{\delta\mathrm{F}} \right)
\end{bmatrix}.
\tag{B.5}
$$

Here, $u_l{}^{\delta\mathrm{F}}$, $u_r{}^{\delta\mathrm{F}}$, $u_b{}^{\delta\mathrm{F}}$, $u_t{}^{\delta\mathrm{F}}$ are the interpolated discontinuous solution-values at the flux-points of the left, right, bottom and top faces of C_O. Also, $\hat{h}_l$, $\hat{h}_r$, $\hat{h}_b$ and $\hat{h}_t$ are the derivatives (in reference-space) of the correction-functions associated with the left, right, bottom and top faces respectively of C_O. These derivatives are taken along the appropriate coordinate-direction in reference-space out of $\hat{x}_1$, $\hat{x}_2$ and $\hat{x}_3$. That is, the correction-functions associated with the left and right faces are differentiated with respect to $\hat{x}_1$, those with the top and bottom faces are differentiated with respect to $\hat{x}_2$, and the remaining two with respect to $\hat{x}_3$. Reintroducing subscripts for clarity, the common interface values $u_l{}^{\delta\mathrm{I}}$, $u_r{}^{\delta\mathrm{I}}$, $u_b{}^{\delta\mathrm{I}}$, $u_t{}^{\delta\mathrm{I}}$ are calculated as

$$
\begin{aligned}
u_l{}^{\delta\mathrm{I}} &= u_{\mathrm{O}l}{}^{\delta\mathrm{I}} = \{u\}_{\mathrm{O}l,\mathrm{L}r} - \beta[\![u]\!]_{\mathrm{O}l,\mathrm{L}r}, \\
u_r{}^{\delta\mathrm{I}} &= u_{\mathrm{O}r}{}^{\delta\mathrm{I}} = \{u\}_{\mathrm{O}r,\mathrm{R}l} + \beta[\![u]\!]_{\mathrm{O}r,\mathrm{R}l}, \\
u_b{}^{\delta\mathrm{I}} &= u_{\mathrm{O}b}{}^{\delta\mathrm{I}} = \{u\}_{\mathrm{O}b,\mathrm{B}t} - \beta[\![u]\!]_{\mathrm{O}b,\mathrm{B}t}, \\
u_t{}^{\delta\mathrm{I}} &= u_{\mathrm{O}t}{}^{\delta\mathrm{I}} = \{u\}_{\mathrm{O}t,\mathrm{T}b} + \beta[\![u]\!]_{\mathrm{O}t,\mathrm{T}b},
\end{aligned}
\tag{B.6}
$$

where β is the upwinding parameter of the LDG viscous-flux. At this stage, we have everything to compute $\boldsymbol{F}^{\delta\mathrm{D}}$ and $\boldsymbol{G}^{\delta\mathrm{D}}$ for C_O. These are also computed for C_L, C_R, C_B and C_T. We now turn to the remaining terms of (B.3); similar to (B.5), the gradients of the inviscid- and viscous-flux-corrections in reference space are calculated as

$$
d\hat{\boldsymbol{F}}^{\delta\mathrm{C}} =
\begin{bmatrix}
\hat{h}_l \left(F_{1,l}{}^{\delta\mathrm{I}} - F_{1,l}{}^{\delta\mathrm{F}} \right) & \hat{h}_l \left(F_{2,l}{}^{\delta\mathrm{I}} - F_{2,l}{}^{\delta\mathrm{F}} \right) \\
\quad + \hat{h}_r \left(F_{1,r}{}^{\delta\mathrm{I}} - F_{1,r}{}^{\delta\mathrm{F}} \right) & \quad + \hat{h}_r \left(F_{2,r}{}^{\delta\mathrm{I}} - F_{2,r}{}^{\delta\mathrm{F}} \right) \\
\hat{h}_b \left(F_{1,b}{}^{\delta\mathrm{I}} - F_{1,b}{}^{\delta\mathrm{F}} \right) & \hat{h}_b \left(F_{2,b}{}^{\delta\mathrm{I}} - F_{2,b}{}^{\delta\mathrm{F}} \right) \\
\quad + \hat{h}_t \left(F_{1,t}{}^{\delta\mathrm{I}} - F_{1,t}{}^{\delta\mathrm{F}} \right) & \quad + \hat{h}_t \left(F_{2,t}{}^{\delta\mathrm{I}} - F_{2,t}{}^{\delta\mathrm{F}} \right)
\end{bmatrix},
\tag{B.7}
$$

and

$$d\hat{\boldsymbol{G}}^{\delta\mathrm{C}} = \begin{bmatrix} \hat{h}_l\left(G_{1,l}{}^{\delta\mathrm{I}} - G_{1,l}{}^{\delta\mathrm{F}}\right) & \hat{h}_l\left(G_{2,l}{}^{\delta\mathrm{I}} - G_{2,l}{}^{\delta\mathrm{F}}\right) \\ \quad + \hat{h}_r\left(G_{1,r}{}^{\delta\mathrm{I}} - G_{1,r}{}^{\delta\mathrm{F}}\right) & \quad + \hat{h}_r\left(G_{2,r}{}^{\delta\mathrm{I}} - G_{2,r}{}^{\delta\mathrm{F}}\right) \\ & \\ \hat{h}_b\left(G_{1,b}{}^{\delta\mathrm{I}} - G_{1,b}{}^{\delta\mathrm{F}}\right) & \hat{h}_b\left(G_{2,b}{}^{\delta\mathrm{I}} - G_{2,b}{}^{\delta\mathrm{F}}\right) \\ \quad + \hat{h}_t\left(G_{1,t}{}^{\delta\mathrm{I}} - G_{1,t}{}^{\delta\mathrm{F}}\right) & \quad + \hat{h}_t\left(G_{2,t}{}^{\delta\mathrm{I}} - G_{2,t}{}^{\delta\mathrm{F}}\right) \end{bmatrix}. \tag{B.8}$$

The $(\cdot)^{\delta\mathrm{F}}$ terms in (B.7) and (B.8) are the interpolated discontinuous flux-values at the flux-points. For the common interface values of the inviscid flux, we use a simple upwind treatment as

$$\begin{bmatrix} F_{1,l}{}^{\delta\mathrm{I}} \\ F_{2,l}{}^{\delta\mathrm{I}} \end{bmatrix} = \bar{\boldsymbol{n}}_l \cdot \partial_u \boldsymbol{F}\left(\{u\}_{\mathrm{O}l,\mathrm{L}r} - \mathrm{sgn}\left(\bar{\boldsymbol{n}}_l \cdot \partial_u \boldsymbol{F}\right) \alpha[\![u]\!]_{\mathrm{O}l,\mathrm{L}r}\right) \bar{\boldsymbol{n}}_l,$$

$$\begin{bmatrix} F_{1,r}{}^{\delta\mathrm{I}} \\ F_{2,r}{}^{\delta\mathrm{I}} \end{bmatrix} = \bar{\boldsymbol{n}}_r \cdot \partial_u \boldsymbol{F}\left(\{u\}_{\mathrm{O}r,\mathrm{R}l} + \mathrm{sgn}\left(\bar{\boldsymbol{n}}_r \cdot \partial_u \boldsymbol{F}\right) \alpha[\![u]\!]_{\mathrm{O}r,\mathrm{R}l}\right) \bar{\boldsymbol{n}}_r,$$

$$\begin{bmatrix} F_{1,b}{}^{\delta\mathrm{I}} \\ F_{2,b}{}^{\delta\mathrm{I}} \end{bmatrix} = \bar{\boldsymbol{n}}_b \cdot \partial_u \boldsymbol{F}\left(\{u\}_{\mathrm{O}b,\mathrm{B}t} - \mathrm{sgn}\left(\bar{\boldsymbol{n}}_b \cdot \partial_u \boldsymbol{F}\right) \alpha[\![u]\!]_{\mathrm{O}b,\mathrm{B}t}\right) \bar{\boldsymbol{n}}_b, \tag{B.9}$$

$$\begin{bmatrix} F_{1,t}{}^{\delta\mathrm{I}} \\ F_{2,t}{}^{\delta\mathrm{I}} \end{bmatrix} = \bar{\boldsymbol{n}}_t \cdot \partial_u \boldsymbol{F}\left(\{u\}_{\mathrm{O}t,\mathrm{T}b} + \mathrm{sgn}\left(\bar{\boldsymbol{n}}_t \cdot \partial_u \boldsymbol{F}\right) \alpha[\![u]\!]_{\mathrm{O}t,\mathrm{T}b}\right) \bar{\boldsymbol{n}}_t,$$

where $\partial_u \boldsymbol{F}$ is the jacobian of the inviscid flux. The common interface values of the viscous-flux are calculated using the LDG-flux as

$$\begin{bmatrix} G_{1,l}{}^{\delta\mathrm{I}} \\ G_{2,l}{}^{\delta\mathrm{I}} \end{bmatrix} = \bar{\boldsymbol{n}}_l \cdot \left(\{\boldsymbol{G}^{\delta\mathrm{F}}\}_{\mathrm{O}l,\mathrm{L}r} + \beta\bar{\boldsymbol{n}}_l\left([\![\boldsymbol{G}^{\delta\mathrm{F}}]\!]_{\mathrm{O}l,\mathrm{L}r} \cdot \bar{\boldsymbol{n}}_l\right) - \tau[\![u]\!]_{\mathrm{O}l,\mathrm{L}r}\bar{\boldsymbol{n}}_l\right) \bar{\boldsymbol{n}}_l,$$

$$\begin{bmatrix} G_{1,r}{}^{\delta\mathrm{I}} \\ G_{2,r}{}^{\delta\mathrm{I}} \end{bmatrix} = \bar{\boldsymbol{n}}_r \cdot \left(\{\boldsymbol{G}^{\delta\mathrm{F}}\}_{\mathrm{O}r,\mathrm{R}l} - \beta\bar{\boldsymbol{n}}_r\left([\![\boldsymbol{G}^{\delta\mathrm{F}}]\!]_{\mathrm{O}r,\mathrm{R}l} \cdot \bar{\boldsymbol{n}}_r\right) + \tau[\![u]\!]_{\mathrm{O}r,\mathrm{R}l}\bar{\boldsymbol{n}}_r\right) \bar{\boldsymbol{n}}_r,$$

$$\begin{bmatrix} G_{1,b}{}^{\delta\mathrm{I}} \\ G_{2,b}{}^{\delta\mathrm{I}} \end{bmatrix} = \bar{\boldsymbol{n}}_b \cdot \left(\{\boldsymbol{G}^{\delta\mathrm{F}}\}_{\mathrm{O}b,\mathrm{B}t} + \beta\bar{\boldsymbol{n}}_b\left([\![\boldsymbol{G}^{\delta\mathrm{F}}]\!]_{\mathrm{O}b,\mathrm{B}t} \cdot \bar{\boldsymbol{n}}_b\right) - \tau[\![u]\!]_{\mathrm{O}b,\mathrm{B}t}\bar{\boldsymbol{n}}_b\right) \bar{\boldsymbol{n}}_b, \tag{B.10}$$

$$\begin{bmatrix} G_{1,t}{}^{\delta\mathrm{I}} \\ G_{2,t}{}^{\delta\mathrm{I}} \end{bmatrix} = \bar{\boldsymbol{n}}_t \cdot \left(\{\boldsymbol{G}^{\delta\mathrm{F}}\}_{\mathrm{O}t,\mathrm{T}b} - \beta\bar{\boldsymbol{n}}_t\left([\![\boldsymbol{G}^{\delta\mathrm{F}}]\!]_{\mathrm{O}t,\mathrm{T}b} \cdot \bar{\boldsymbol{n}}_t\right) + \tau[\![u]\!]_{\mathrm{O}t,\mathrm{T}b}\bar{\boldsymbol{n}}_t\right) \bar{\boldsymbol{n}}_t,$$

where τ is the jump-penalization parameter of the LDG-flux. Plugging everything back into (B.2) and rearranging gives the semi-discrete form

$$\partial_t u = \mathfrak{P}_{\mathrm{O}} u_{\mathrm{O}}{}^{\delta\mathrm{D}} + \mathfrak{P}_{\mathrm{L}} u_{\mathrm{L}}{}^{\delta\mathrm{D}} + \mathfrak{P}_{\mathrm{R}} u_{\mathrm{R}}{}^{\delta\mathrm{D}} + \mathfrak{P}_{\mathrm{B}} u_{\mathrm{B}}{}^{\delta\mathrm{D}} + \mathfrak{P}_{\mathrm{T}} u_{\mathrm{T}}{}^{\delta\mathrm{D}}$$

$$+ \mathfrak{P}_{\mathrm{LL}} u_{\mathrm{LL}}{}^{\delta\mathrm{D}} + \mathfrak{P}_{\mathrm{RR}} u_{\mathrm{RR}}{}^{\delta\mathrm{D}} + \mathfrak{P}_{\mathrm{BB}} u_{\mathrm{BB}}{}^{\delta\mathrm{D}} + \mathfrak{P}_{\mathrm{TT}} u_{\mathrm{TT}}{}^{\delta\mathrm{D}} \tag{B.11}$$

$$+ \mathfrak{P}_{\mathrm{LB}} u_{\mathrm{LB}}{}^{\delta\mathrm{D}} + \mathfrak{P}_{\mathrm{LT}} u_{\mathrm{LT}}{}^{\delta\mathrm{D}} + \mathfrak{P}_{\mathrm{RB}} u_{\mathrm{RB}}{}^{\delta\mathrm{D}} + \mathfrak{P}_{\mathrm{RT}} u_{\mathrm{RT}}{}^{\delta\mathrm{D}},$$

where the $\mathfrak{P}_i$ matrix contains all operations applied on the discontinuous solution $u_i{}^{\delta\mathrm{D}}$ in cell C_i. This equation is then used in the main text in Sub-section 3.1.

Appendix C. Assembly of result-plots in Section 3

The plots used in Section 3 present an overview of the behavior of the different length-scale strategies over a wide range of cases involving variation of meshes, polynomial-orders, incidence-angles and trial-solution wavenumbers. Hence, they condense a
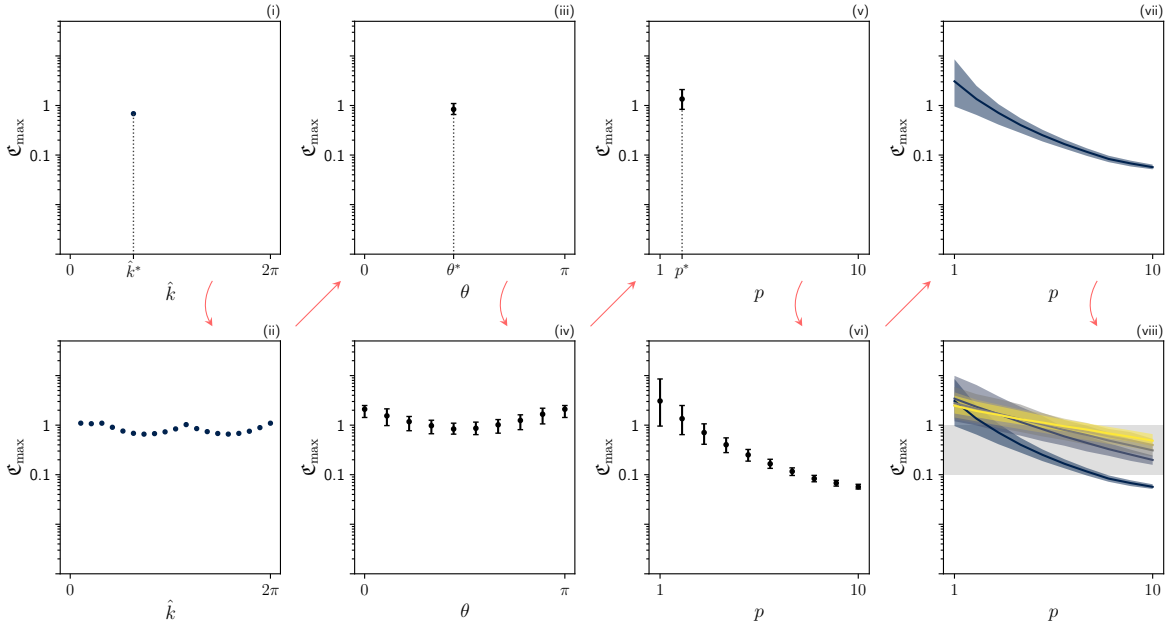
Fig. C.16: Steps involved in construction of the CFL-variation plots in Figure 7, Figure 8 and Figure 9. (i) For fixed choices of mesh (M_5^a), $p = p^*$, $\theta = \theta^*$ and $\hat{k} = \hat{k}^*$, the resulting $\mathfrak{C}_{max}$ is a scalar value on an abcissa of $\hat{k}$. (ii) Keeping all else fixed, $\hat{k}$ is varied over its range, leading to a series of $\mathfrak{C}_{max}$ values. (iii) On a plot of θ-abcissa, at $\theta = \theta^*$, this variation of $\mathfrak{C}_{max}$ with $\hat{k}$ is collapsed into a variation-bar around the mean-value. (iv) Keeping the mesh and p fixed, this variation is plotted over the range of θ. (v) On a plot of p-abcissa, at $p = p^*$, this variation of $\mathfrak{C}_{max}$ with both $\hat{k}$ and θ is collapsed into a variation-bar around the mean-value. (vi) Keeping the mesh fixed, this variation is plotted over the range of p. (vii) For better visibility, the plot from vi is converted into a filled range-plot, with the solid-line representing the mean-values. (viii) Finally, such plots are generated for all meshes involved in that study.

584   lot of information into a consumable and interpretable form. This appendix explains the steps of this condensation, with the hope

585   that the reader can better grasp the extent of information encapsulated in them.

586   As an example, we reconstruct in Figure C.16 the sub-plot from Figure 7 corresponding to Pe $= 10^3$ for the GS1 strategy

587   (fourth column, second row). Recall, that this sub-plot shows the variation of $\mathfrak{C}_{max}$ with polynomial-orders on different shear-

588   skewed meshes (represented by colors). Also recall, that the variation with $\hat{k}$ and θ is captured in the width of colored band.

589   • Let us begin with a single value of each parameter - we choose mesh M_5^a, $p = p^* = 2$, $\theta = \theta^* = 80°$ and $\hat{k} = \hat{k}^* = 0.6\pi$. The

590   corresponding $\mathfrak{C}_{max}$ for this configuration is a scalar value, which is plotted in (i).

591   • Next, keeping the mesh, p^* and θ^*, we obtain a scalar value of $\mathfrak{C}_{max}$ corresponding to each value of $\hat{k}$ that we test - this series

592   of $\mathfrak{C}_{max}$-variation with $\hat{k}$ is plotted in (ii).

593   • On a plot where the abcissa is θ, this variation can be collapsed into variation around a mean-value, located at $\theta = \theta^*$. This

594   is plotted in (iii)

595   • Keeping the mesh and p^* fixed, such variation can be obtained in a similar manner for other values of θ. This is plotted in
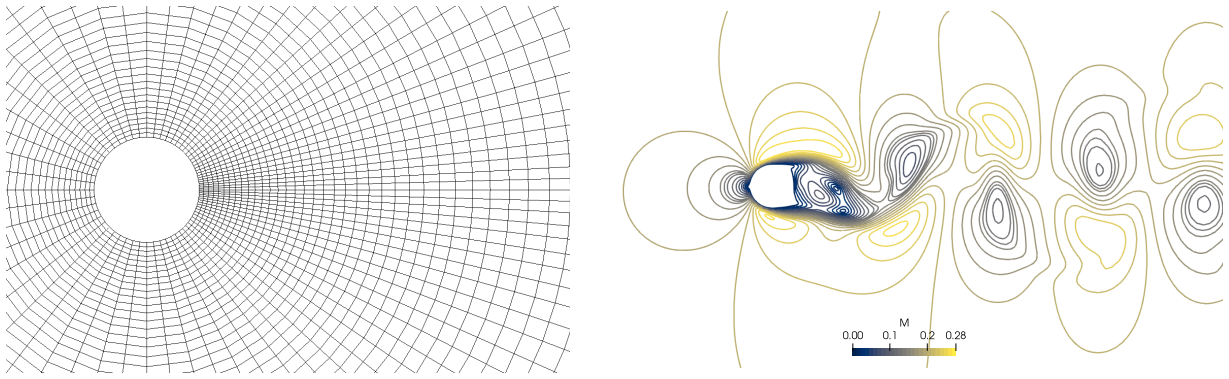
596   (iv).

Fig. D.17: (Left) 2nd-order quadrilateral mesh with 7488 elements used for the simulations of Appendix D. (Right) Contours of Mach-number for Re = 150 and M = 0.2.

- Continuing, on a plot where the abcissa is p, the aforementioned variation of $\mathfrak{C}_{\mathrm{max}}$ with both $\hat{k}$ and θ can be collapsed into variation around a mean-value, located at $p = p^*$. This is plotted in (v).

- Keeping the mesh fixed, such variation can be similarly obtained for other values of p, as plotted in (vi).

- For better visibility, the variation-bars are replaced in (vii) with a filled range-plot. The mean-values are plotted as a solid line.

- Finally, such plots are generated for other meshes involved in the study, as in (viii). Different meshes are represented by different colors, with yellow being of highest quality and blue being of the lowest.

This completes the generation of the sub-plot. A similar procedure is followed for the generation of other plots where variation is encapsulated in filled range-plots.

Appendix D. Absence of spurious oscillations near stability limit

To demonstrate the absence of spurious oscillations near the stability limit, we simulate flow around a cylinder in 2D at Re = 150 and M = 0.2 [35]. The mesh is of O-shape and comprises of 7488 second-order quadrilaterals (see Figure D.17), with no-slip adiabatic wall boundary-condition on the cylinder surface and characteristic boundary-condition on the outer boundaries. Simulations are run at $p \in [2, 4]$ with $\mathfrak{C}$ of 1.1 for $p = 2$, and 1 for $p = 3$ and $p = 4$. Pushing $\mathfrak{C}$ beyond stated limits leads to instability and eventual blow-up. The contours of Mach-number are shown in Figure D.17. The resulting Strouhal number (St) is 0.18298, 0.18304 and 0.18311 respectively, which matches well with the value of 0.1831 from high-order finite-difference simulations by Müller [35]. Thus, we see that, within stability limits, no spurious oscillations are introduced.

References

[1] J. Slotnick, A. Khodadoust, J. Alonso, D. Darmofal, W. Gropp, E. Lurie, D. Mavriplis, CFD vision 2030 study: a path to revolutionary computational aerosciences, 2014.

[2] H. K. Versteeg, W. Malalasekera, An introduction to computational fluid dynamics: the finite volume method, Pearson education, 2007.

[3] N. Fehn, P. Munch, W. A. Wall, M. Kronbichler, Hybrid multigrid methods for high-order discontinuous Galerkin discretizations, Journal of Computational Physics 415 (2020) 109538.

[4] B. Cockburn, S.-Y. Lin, C.-W. Shu, TVB Runge-Kutta local projection discontinuous Galerkin finite element method for conservation laws iii: One-dimensional systems, Journal of Computational Physics 84 (1989) 90–113.

[5] B. Cockburn, C. Shu, Runge-Kutta discontinuous Galerkin methods for convection-dominated problems, Journal of Scientific Computing 16 (2001) 173–261.

[6] W. Trojak, R. Watson, A. Scillitoe, P. G. Tucker, Effect of Mesh Quality on Flux Reconstruction in Multi-dimensions, Journal of Scientific Computing 82 (2020) 77.

[7] J. S. Hesthaven, T. Warburton, Nodal discontinuous Galerkin methods: algorithms, analysis, and applications, Springer Science & Business Media, 2007.

[8] G. Karniadakis, S. Sherwin, Spectral/hp element methods for computational fluid dynamics, Oxford University Press, 2013.

[9] D. Dutykh, How to overcome the Courant-Friedrichs-Lewy condition of explicit discretizations?, arXiv preprint arXiv:1611.09646 (2016).

[10] N. A. Loppi, F. D. Witherden, A. Jameson, P. E. Vincent, Locally adaptive pseudo-time stepping for high-order Flux Reconstruction, Journal of Computational Physics 399 (2019) 108913.

[11] T. Toulorge, W. Desmet, CFL conditions for Runge-Kutta discontinuous Galerkin methods on triangular grids, Journal of Computational Physics 230 (2011) 4657–4678.

[12] G. Gassner, F. Lörcher, C.-D. Munz, A discontinuous Galerkin scheme based on a space-time expansion ii. Viscous flow equations in multi dimensions, Journal of Scientific Computing 34 (2008) 260–286.

[13] H. Huynh, On explicit discontinuous Galerkin methods for conservation laws, Computers & Fluids 222 (2021) 104920.

[14] N. Chalmers, L. Krivodonova, A robust CFL condition for the discontinuous Galerkin method on triangular meshes, Journal of Computational Physics 403 (2020) 109095.

[15] J. Watkins, K. Asthana, A. Jameson, A numerical analysis of the nodal discontinuous Galerkin scheme via Flux Reconstruction for the advection-diffusion equation, Computers Fluids 139 (2016) 233–247. 13th USNCCM International Symposium of High-Order Methods for Computational Fluid Dynamics.

[16] F. Trias, O. Lehmkuhl, A self-adaptive strategy for the time integration of Navier-Stokes equations, Numerical Heat Transfer, Part B: Fundamentals 60 (2011) 116–134.

[17] H. T. Huynh, A flux reconstruction approach to high-order schemes including discontinuous Galerkin methods, in: 18th AIAA Computational Fluid Dynamics Conference, 2007, p. 4079.

[18] B. Cockburn, C.-W. Shu, The local discontinuous Galerkin method for time-dependent convection-diffusion systems, SIAM Journal on Numerical Analysis 35 (1998) 2440–2463.

[19] P. Castonguay, High-order energy stable flux reconstruction schemes for fluid flow simulations on unstructured grids, Stanford University, 2012.

[20] O. Knoth, J. Wensch, Generalized split-explicit runge–kutta methods for the compressible euler equations, Monthly Weather Review 142 (2014) 2067–2081.

[21] D. I. Ketcheson, Runge–kutta methods with minimum storage implementations, Journal of Computational Physics 229 (2010) 1763–1773.

[22] J. Manzanero, G. Rubio, E. Ferrer, E. Valero, Dispersion-dissipation analysis for advection problems with nonconstant coefficients: applications to discontinuous Galerkin formulations, SIAM Journal on Scientific Computing 40 (2018) A747–A768.

[23] J. Kou, A. Hurtado-de Mendoza, S. Joshi, S. Le Clainche, E. Ferrer, Eigensolution analysis of immersed boundary method based on volume penalization: applications to high-order schemes, Journal of Computational Physics 449 (2022) 110817.

[24] J. Kou, S. Le Clainche, E. Ferrer, Data-driven eigensolution analysis based on a spatio-temporal Koopman decomposition, with applications to high-order methods, Journal of Computational Physics 449 (2022) 110798.

[25] A. Hurtado-de Mendoza, J. Kou, S. Joshi, K. Puri, C. Hirsch, E. Ferrer, Non-modal analysis of linear multigrid schemes for the high-order Flux Reconstruction method, Journal of Computational Physics 456 (2022) 111070.

[26] P. D. Lax, R. D. Richtmyer, Survey of the stability of linear finite difference equations, Communications on pure and applied mathematics 9 (1956) 267–293.

[27] D. A. Kopriva, Implementing spectral methods for partial differential equations: Algorithms for scientists and engineers, Springer Science & Business Media, 2009.

[28] H. Schlichting, K. Gersten, Boundary-Layer Theory, 8th ed., Springer, 2000. URL: `http://dx.doi.org/10.1007/978-3-642-85829-1`.

[29] S. R. Allmaras, F. T. Johnson, Modifications and clarifications for the implementation of the Spalart-Allmaras turbulence model, in: Seventh international conference on computational fluid dynamics (ICCFD7), volume 1902, Big Island, HI, 2012.

[30] K. J. Fidkowski, T. A. Oliver, J. Lu, D. L. Darmofal, p-Multigrid solution of high-order discontinuous Galerkin discretizations of the compressible navier–stokes equations, Journal of Computational Physics 207 (2005) 92–113.

[31] C. Hirsch, Numerical computation of internal and external flows. Volume 1: Fundamentals of computational fluid dynamics, Elsevier, 1988.

[32] C. Hirsch, Numerical computation of internal and external flows. Volume 2: Computational methods for inviscid and viscous flows, John Wiley Sons, 1990.

[33] G. Mengaldo, D. De Grazia, F. Witherden, A. Farrington, P. Vincent, S. Sherwin, J. Peiro, A guide to the implementation of boundary conditions in compact high-order methods for compressible aerodynamics, in: 7th AIAA Theoretical Fluid Mechanics Conference, 2014, p. 2923.

[34] International workshop on high-order CFD methods, `https://www1.grc.nasa.gov/research-and-engineering/hiocfd/#c3-difficult-2d-3d`, 2015. [Online; accessed 17-Nov-2021].

[35] B. Müller, High order numerical simulation of aeolian tones, Computers & Fluids 37 (2008) 450–462.